LUND UNIVERSITY

Computational and experimental methods for imaging and dosimetry in 177Lu radionuclide therapy

Classical and novel gamma cameras

Roth, Daniel

2021

Computational and experimental methods for imaging and dosimetry in ^{177}Lu radionuclide therapy

Classical and novel gamma cameras

DANIEL ROTH
DEPARTMENT OF MEDICAL RADIATION PHYSICS | LUND UNIVERSITY

Computational and experimental methods for imaging and dosimetry in ^{177}Lu radionuclide therapy

Computational and experimental methods for imaging and dosimetry in ^{177}Lu radionuclide therapy

Classical and novel gamma cameras

by Daniel Roth

LUND
UNIVERSITY

Thesis for the degree of Doctor of Philosophy
Thesis advisors: Prof. Katarina Sjögreen-Gleisner, Dr. Erik Larsson
Faculty opponent: Dr. Kjell Erlandsson, Institute of Nuclear Medicine,
University College London, UK

Organization	Document name
LUND UNIVERSITY	**DOCTORAL DISSERTATION**
Department of Medical Radiation Physics Skåne University Hospital, Lund SE–221 85 LUND Sweden	Date of disputation 2020-05-28
	Sponsoring organization

Author(s)
Daniel Roth

Title and subtitle
Computational and experimental methods for imaging and dosimetry in ^{177}Lu radionuclide therapy: Classical and novel gamma cameras

Abstract

Radionuclide therapy (RNT) is a form of radiotherapy that uses unsealed radioactive sources for the delivery of ionising radiation within a patient's body. Radiation dosimetry is not used routinely in all centres, and the RNT field can benefit from more data on pharmacokinetics and absorbed doses (ADs). Consequently, there is a value in developing and investigating methods that facilitates the acquirement of pharmacokinetic data and AD calculation.

Papers I and IV focus on tumour dosimetry in peptide receptor radionuclide therapy (PRRT) with [^{177}Lu]Lu-DOTA-TATE. In Paper I, a method for tumour dosimetry was developed, with the intention to be applicable to image sets consisting of a combination of planar and single photon emission computed tomography (SPECT) images. Semi-automatic segmentation methods are developed and employed for robustness and to alleviate the operator workload. Evaluation showed that the dosimetry method worked well provided that tumour selection criteria were applied. In Paper IV, this method was applied across all treatment cycles in a larger set of patients, producing a large collection of ADs and pharmacokinetics data for tumours. Analysis showed how the ADs evolved over treatment cycles and how this could be explained by changes in the pharmacokinetic parameters, findings which in the long run could help in the design of new treatment and imaging protocols.

Papers II, III and V focus on a cadmium zinc telluride (CZT)-based hand-held gamma camera and lay the groundwork for its application within RNT. In Paper II, the camera was characterised and the feasibility of using it for ^{177}Lu imaging was investigated. We found that it was capable of producing useful images and identified appropriate collimators and energy windows. In Paper III, we sought to improve the understanding of how the energy-tailing associated with the CZT-crystal affected ^{177}Lu imaging with the help of Monte Carlo simulations. The wide range of energies of interest for ^{177}Lu meant that new model of the camera system had to be developed and tuned to reproduce the camera's behaviour. Through the model, we were able to gain a better understanding of the camera and estimate the interference of higher-energy photons on lower energy windows. In Paper V, we aimed to develop a method with which the camera could be used for activity quantification. This was done by adapting a dual-photopeak method to ^{177}Lu, a method in which measurements over multiple photopeaks are employed to infer the depth of a source, allowing for activity-quantification with attenuation-correction.

Key words
Radionuclide therapy, [^{177}Lu]Lu-DOTA-TATE, Gamma camera imaging, Activity quantification, Dosimetry, CdZnTe, Monte Carlo modelling

Classification system and/or index terms (if any)

Supplementary bibliographical information	Language English

ISSN and key title	ISBN 978-91-7895-849-8 (print) 978-91-7895-850-4 (pdf)

Recipient's notes	Number of pages 99	Price
	Security classification	

I, the undersigned, being the copyright owner of the abstract of the above-mentioned dissertation, hereby grant to all reference sources the permission to publish and disseminate the abstract of the above-mentioned dissertation.

Signature *Daniel Roth*

Date ___2021-04-19___

DOKUMENTDATABLAD enl SIS 61 41 21

Computational and experimental methods for imaging and dosimetry in ^{177}Lu radionuclide therapy

Classical and novel gamma cameras

by Daniel Roth

LUND
UNIVERSITY

A doctoral thesis at a university in Sweden takes either the form of a single, cohesive research study (monograph) or a summary of research papers (compilation thesis), which the doctoral student has written alone or together with one or several other author(s).

In the latter case the thesis consists of two parts. An introductory text puts the research work into context and summarizes the main points of the papers. Then, the research publications themselves are reproduced, together with a description of the individual contributions of the authors. The research papers may either have been already published or are manuscripts at various stages (in press, submitted, or in draft).

Cover illustration front: A collection of signal pulses from a model of a pixelated CZT detector.

Science isn't about WHY. It's about WHY NOT.
— Cave Johnson – Portal 2

Contents

Abbreviations

AD   absorbed dose

AHASA   as high as safely attainable

ASIC   application-specific integrated circuit

CIE   charge induction efficiency

CT   computed tomography

CZT   cadmium zinc telluride

EBRT   external beam radiotherapy

FOV   field of view

FWHM   full width at half maximum

LEHR   low energy high resolution

LEHS   low energy high sensitivity

MCA   multichannel analyser

MEGP   medium energy general purpose

MIRD medical internal radiation dose

ML-EM maximum likelihood expectation maximization

MRI magnetic resonance imaging

MRT molecular radiotherapy

NET neuroendocrine tumour

NaI(Tl) thallium-doped sodium-iodide

PET positron emission tomography

PM photomultiplier

PRRT peptide receptor radionuclide therapy

PSF point-spread function

PVE partial volume effect

RC recovery coefficient

RNT radionuclide therapy

SPECT single photon emission computed tomography

SUV standardised uptake value

TEW triple energy window

List of original papers

This thesis is based on the following publications, referred to by their Roman numerals:

I **A method for tumor dosimetry based on hybrid planar-SPECT/CT images and semiautomatic segmentation**
D. Roth, J. Gustafsson, A. Sundlöv and K. Sjögreen Gleisner
Medical Physics, 2018, **45**, pp. 5004–5018

II **Characterisation of a hand-held CZT-based gamma camera for ^{177}Lu imaging**
D. Roth, E. Larsson, A. Sundlöv and K. Sjögreen Gleisner
EJNMMI Physics, 2020, **7**, article number 46

III **Modelling of a CZT-based gamma camera with application to ^{177}Lu imaging**
D. Roth, E. Larsson, M. Ljungberg and K. Sjögreen Gleisner
Manuscript, to be submitted to Medical Physics

IV **Dosimetric quantities of neuroendocrine tumors over treatment cycles with ^{177}Lu-DOTA-TATE**
D. Roth*, J. Gustafsson*, C.F. Warfvinge, A. Sundlöv, A. Åkesson, J. Tennvall, K. Sjögreen Gleisner
Manuscript submitted to Journal of Nuclear Medicine, under revision

V **Feasibility of ^{177}Lu activity quantification using a CZT-based hand-held gamma camera**
D. Roth, E. Larsson and K. Sjögreen Gleisner
Manuscript

Paper I: © American Association of Physicists in Medicine. Reprinted with permission.

Paper II: © The Authors (Open Access).

List of contributions

Co-authors are abbreviated as follows:
Daniel Roth (DR), Katarina Sjögreen Gleisner (KSG), Johan Gustafsson (JG),
Anna Sundlöv (AS), Erik Larsson (EL), Michael Ljungberg (MLj), Carl Fredrik Warfvinge
(CFW), Anna Åkesson (AÅ), Jan Tennvall (JT).

Paper I: A method for tumor dosimetry based on hybrid planar-SPECT/CT images and semiautomatic segmentation

I developed the planar image segmentation method and implemented the computer code and graphical user interface for it. I applied the dosimetry method on the patient and phantom images and evaluated the acquired data. I drafted the manuscript and was the main and corresponding author.

Paper II: Characterisation of a hand-held CZT-based gamma camera for ^{177}Lu imaging

I made the majority of the experimental design and performed the data collection. I developed computer code to read, analyse and interpret the measured data. I drafted the manuscript and was the main and corresponding author.

Paper III: Modelling of a CZT-based gamma camera with application to ^{177}Lu imaging

I had the initial idea of modelling charge transport and signal generation in the CZT crystal and developed the computer code to make the necessary calculations. I developed the code to integrate the results into a full camera model, along with the code to tune this model. I also performed the experimental measurements and computer simulations. I drafted the manuscript and am the main author.

Paper IV: Dosimetric quantities of neuroendocrine tumors over treatment cycles with ^{177}Lu-DOTA-TATE

I developed a user program that was central to data organisation and dosimetry in the project. I had a supervisory role when this program was used to gather tumour dosimetry

data, participated in the data verification, and performed the data cleaning. I designed, 3D-printed and analysed the spheres underlying the recovery correction. I developed computer code that gathered and prepared the data used in the statistical analysis. I reviewed the statistical analysis code, contributed to the manuscript writing, review and commenting. I share first authorship with JG.

Paper v: Feasibility of ^{177}Lu activity quantification using a CZT-based hand-held gamma camera

I participated in the design and development of the activity quantification method. I designed and performed all experimental measurements. I implemented the computer code for the quantification method and the evaluation thereof. I contributed to the manuscript draft and am the main author.

Summary

Radionuclide therapy (RNT) is a form of radiotherapy that uses unsealed radioactive sources for the delivery of ionising radiation within a patient's body. Radiation dosimetry is not used routinely in all centres, and the RNT field can benefit from more data on pharmacokinetics and absorbed doses (ADs). Consequently, there is a value in developing and investigating methods that facilitates the acquirement of pharmacokinetic data and AD calculation.

Papers ɪ and ɪᴠ focus on tumour dosimetry in peptide receptor radionuclide therapy (PRRT) with [^{177}Lu]Lu-DOTA-TATE. In Paper ɪ, a method for tumour dosimetry was developed, with the intention to be applicable to image sets consisting of a combination of planar and single photon emission computed tomography (SPECT) images. Semi-automatic segmentation methods are developed and employed for robustness and to alleviate the operator workload. Evaluation showed that the dosimetry method worked well provided that tumour selection criteria were applied. In Paper ɪᴠ, this method was applied across all treatment cycles in a larger set of patients, producing a large collection of ADs and pharmacokinetics data for tumours. Analysis showed how the ADs evolved over treatment cycles and how this could be explained by changes in the pharmacokinetic parameters, findings which in the long run could help in the design of new treatment and imaging protocols.

Papers ɪɪ, ɪɪɪ and ᴠ focus on a cadmium zinc telluride (CZT)-based hand-held gamma camera and lay the groundwork for its application within RNT. In Paper ɪɪ, the camera was characterised and the feasibility of using it for ^{177}Lu imaging was investigated. We found that it was capable of producing useful images and identified appropriate collimators and energy windows. In Paper ɪɪɪ, we sought to improve the understanding of how the energy-tailing associated with the CZT-crystal affected ^{177}Lu imaging with the help of Monte Carlo simulations. The wide range of energies of interest for ^{177}Lu meant that new model of the camera system had to be developed and tuned to reproduce the camera's behaviour. Through the model, we were able to gain a better understanding of the camera and estimate the interference of higher-energy photons on lower energy windows. In Paper ᴠ, we aimed to develop a method with which the camera could be used for activity quantification. This

was done by adapting a dual-photopeak method to ^{177}Lu, a method in which measurements over multiple photopeaks are employed to infer the depth of a source, allowing for activity-quantification with attenuation-correction.

Sammanfattning på svenska

Radionuklidterapi är en form av strålbehandling där sjukdom behandlas genom att ett radioaktivt ämne tillförs till kroppen. Typiskt sett består det tillförda ämnet av två sammankopplade komponenter: Dels en radionuklid (radioaktiv variant av ett viss grundämne) och dels ett läkemedel vars egenskaper gör att det tas upp i det sjuka området. Ofta tillförs det radioaktiva läkemedlet via injektion i ett blodkärl, efter vilket ämnet cirkulerar runt i kroppen och ackumuleras företrädesvis i det sjuka området och minimalt i normala organ. Radioisotopen avger joniserande strålning som skadar ett omkringliggande område, och ackumulering av skador till det sjuka området ger radionuklidterapin dess behandlande verkan. Joniserande strålnings interaktion med omgivningen kan mätas genom måttet absorberad dos, som anger den totala mängden energi som joniserande strålning har avgett till massan inom ett område. Ofta används en radionuklid som avger joniserande strålning med lagom kort räckvidd så att den större delen av energin absorberas inom ett närliggande område. Vissa radionuklider kan även avge gammastrålning med längre räckvidd, vilket öppnar för möjligheten att avbilda läkemedlets fördelning med en gammakamera.

Radionuklidterapi är någorlunda unikt jämfört med andra former av strålbehandling, på så sätt att den absorberade dosen till sjuka områden och normala organ avgörs av hur patientens kropp tar upp läkemedlet, något som kan variera mellan patienter. Normala organ riskerar att ta viss skada, beroende på hur läkemedlet tas upp i kroppen samt vilken räckvidd den joniserande strålningen har. Det finns därmed möjlighet till att optimera behandlingen genom att justera mängden radioaktivt läkemedel som injiceras så att maximal behandlingseffekt erhålls med minimala sidoeffekter. Att beräkna den absorberade dosen innebär att det radioaktiva läkemedlets tids-beroende cirkulering i kroppen behöver bestämmas. Denna cirkulering studeras ofta genom bildtagningar med en gammakamera vid ett antal tillfällen. Att utföra upprepade biltagningar och analysera bilderna kan dock vara tid- och resurs-krävande för kliniken, samt obekvämt för patienterna. För närvarande finns det begränsat med evidens för att dosberäkningar kan användas för att ge ett mervärde till behandlingar, och många kliniker använder istället förutbestämda doseringar. Det finns därmed ett värde i att utveckla nya metoder som underlättar dosberäkningar eller studerandet av upptaget av läkemedel, så att mer kunskap kan samlas in inom området. På sikt

kan sådan kunskap leda till att individoptimerade behandlingar baserade på dosberäkningar kan introduceras i större utsträckning.

I denna avhandling har mycket fokus lagts på tumörer inom behandling med ett specifikt radioaktivt läkemedel ($[^{177}Lu]$Lu-DOTA-TATE). Inom ett arbete utvecklades och undersöktes en metod för dosberäkning inom ett specifikt bildmaterial. I ett senare arbete applicerades denna metod i en större uppsättning bilder, vilket möjliggjorde en studie av läkemedlets upptag inom tumörer och de resulterade absorberade doserna över många återkommande behandlingar. De tre övriga arbetena fokuserar på en handhållen gammakamera och grunderna läggs för att använda denna inom radionuklidterapi. Kameran är av intresse då det är enkelt att utföra bildtagningar med den, vilket innebär att den skulle kunna användas för att studera upptaget av radioaktiva läkemedel med en större mängd bildtagningar äv vad som är praktiskt med en vanlig gammakamera. Den handhållna kamerans arbeten handlar inledningsvis om karakterisering genom mätningar och datorsimuleringar för att få en bättre förståelse av hur kameran fungerar. Ett slutligt arbete handlar även om utvecklingen av en metod med vilken den absoluta mängden av upptaget radioaktivt läkemedel kan skattas från mätningar kameran.

Chapter 1

Introduction and aim

Radionuclide therapy (RNT) (also called molecular radiotherapy (MRT)) is a treatment modality which employs internally distributed unsealed radioactive substances to treat benign or malignant diseases (Chatal and Hoefnagel, 1999; Dash et al., 2015; Sjögreen Gleisner et al., 2017; Pais et al., 2017). A systemic administration of a radiopharmaceutical consisting of a radionuclide attached to a targeting molecule is a frequently used approach in RNT, which often gives such treatments the combined advantages of being selective (akin to external beam radiotherapy (EBRT)) while simultaneously being capable of treating disseminated disease (akin to chemotherapy) (Chatal and Hoefnagel, 1999; Dash et al., 2015).

Peptide receptor radionuclide therapy (PRRT) is a field of RNT which has been studied and seen as promising since the early 90s (Chatal and Hoefnagel, 1999; Bodei et al., 2011; Cives and Strosberg, 2017). PRRTs utilise the fact that some types of cancer cells have a large overexpression of receptors for certain peptides, which leads to much higher tumour uptakes of associated radiolabelled peptides compared to normal tissue. Neuroendocrine tumours (NETs) is a tumour type which has received a lot of attention in the PRRT field. This tumour type often have an overexpression of somatostatin receptors, which has lead to studies where radiolabelled somatostatin analogues have been used for treatment. Earlier studies used an ^{111}In-labelled peptide, which has been superseded by ^{90}Y- and ^{177}Lu-labelled peptides in later studies (Bodei et al., 2013; Dash et al., 2015). The most frequently used radiopeptide for NETs is currently [^{177}Lu]Lu-DOTA-TATE (Cives and Strosberg, 2017), whose efficacy and tolerability has been demonstrated by the NETTER-1 randomised phase 3 trial (Strosberg et al., 2017).

^{177}Lu is a radionuclide that decays through β^--emission with a half-life of 6.647 d. The β^--emissions make the radionuclide suitable for therapeutic applications. Additionally, gamma photons are emitted as part of the decays, allowing the distribution of a labelled

radiopharmaceutical in a patient to be imaged and quantified. The two most prominent emissions used for imaging have energies and yields of 112.9 keV (6.20 %) and 208.4 keV (10.38 %) (Kellett and Bersillon, 2017). Beyond these two gamma-emissions, there are also notable x-ray emissions at energies of 54.6 keV (1.59 %) and 55.8 keV (2.78 %).

Ionising radiation emitted following radionuclide decay is either fully or partially responsible for the therapeutic effects of RNT (Sjögreen Gleisner et al., 2017). Dosimetry is an important tool for the prediction of the therapeutic effect and toxicity in other forms of radiotherapy, such as EBRT, but does not necessarily have the same status in RNT (Giammarile et al., 2017). Common non-dosimetric methods in RNT instead usually involve the use of fixed amounts of administered activity, or activities scaled by some measure of body size. In the case of [^{177}Lu]Lu-DOTA-TATE therapies, the standard treatment protocol involves the administration of 7.4 GBq approximately every two months for a total of four treatment cycles, without any dosimetric calculations (Strosberg et al., 2017). This type of one-scheme-fits-all approach effectively treats the radiopharmaceutical in a manner similar to regular pharmaceutical prescriptions, and ignores the fact that radiopharmaceuticals can exhibit notable variations in uptake and absorbed doses (ADs) between patients. Current radiobiological knowledge supports the hypothesis that dosimetry can be of benefit for RNT (Flux et al., 2018), and there are ongoing clinical trials of [^{177}Lu]Lu-DOTA-TATE investigating dosimetry-driven individualised treatment protocols (Sundlöv et al., 2017; Garske-Román et al., 2018; Del Prete et al., 2019). Two approaches are presented in these trials: a fixed amount of administered activity (7.4 GBq) per cycle with variable number of cycles delivered (Sundlöv et al., 2017; Garske-Román et al., 2018), or a fixed number of cycles (four) with patient-specific administered activities (Del Prete et al., 2019). In all cases, the treatment protocol follows an as high as safely attainable (AHASA) approach, where as much activity as possible is administered while limits in total ADs to organs at risk (kidneys and bone marrow) are maintained. AD-limits are typically extrapolated from known limits in EBRT, but some AD-effect relationships have been found in PRRT. Found relationships covers ^{90}Y- and ^{177}Lu-based treatments in targets such as kidneys (Barone et al., 2005; Gupta et al., 2012; Bodei et al., 2008), bone marrow (Forrer et al., 2009; Walrand et al., 2011; Svensson et al., 2016; Bergsma et al., 2016; Del Prete et al., 2017), pituitary gland (Sundlöv et al., 2021) and tumours (Pauwels et al., 2005; Ilan et al., 2015; Jahn et al., 2021). To optimise PRRT treatments further, there is a need to gather more data on organ and tumour ADs, AD-effect relationships, and typical behaviours of dosimetric parameters between treatment cycles. Ideally, such information could ultimately be used in the long run to optimise and personalise PRRT therapies further.

The overarching aim of this thesis has been to develop methods for imaging and dosimetric calculations that can be used to advance the knowledge on dosimetry in RNT, with a focus on ^{177}Lu, [^{177}Lu]Lu-DOTA-TATE and NETs. The works in this thesis can be roughly divided into two tracks, both working towards this common aim. The first track comprises

Paper I and Paper IV, and involves the development of a tumour dosimetry method and its application in a set of patient images. The second track comprises Paper II, Paper III and Paper V, and involves the investigation of a hand-held gamma camera and its applicability to imaging and activity quantification of ^{177}Lu. Summarising, the specific aims of the works in the thesis can be listed as

- Develop a practical method and workflow for tumour dosimetry within the context of the imaging protocol of a clinical study (Sundlöv et al., 2017), and investigate the viability of the method (Paper I).

- Apply the dosimetry method to a larger set of patient images to produce a a large collection of tumour-ADs, laying the groundwork for a future investigation of tumour AD-effects relationships, and, in the interim, study the evolution of ADs and dosimetric parameters across treatment cycles (Paper IV).

- Characterise a hand-held cadmium zinc telluride (CZT)-based gamma camera and investigate the possibility of using it for ^{177}Lu imaging (Paper II). Building on the characterisation, gain further understanding of the cameras CZT-related behaviours by developing a model of the signal-generation processes and linking the model to Monte Carlo simulations (Paper III).

- Develop and evaluate a method for activity quantification with the hand-held gamma camera (Paper V).

Chapter 2

Imaging in nuclear medicine

1   The gamma camera

In nuclear medicine, imaging is performed using gamma cameras. These are instruments capable of detecting high-energy photons (x-rays or gamma photons), producing images of the incident radiation fluence. In many cases in nuclear medicine, imaging is integral to achieving a set task, such as establishing a diagnosis or estimating radiation doses with sufficient accuracy.

The starting point for imaging in nuclear medicine is the administration of a pharmaceutical labelled with a radionuclide, the decay of which yields x-rays or gamma photons. The fundamental requirement for a gamma camera is to be able to determine both the energy and the point of interaction for the incident photons. Spectroscopic capabilities are achieved using the same principles as for non-imaging radiation-spectrometers. For this purpose, the gamma camera is typically centred around a scintillation or semiconductor crystal, the properties of which allow the energy deposited by incident radiation to be converted into more easily measurable quantities, such as flashes of visible light or electrical currents. Position estimation is typically achieved by attaching an array of sensors to the crystal surface and inferring interaction points through the position and signal of one, a few or all of the sensors. Figure 2.1 presents a cross-section of the arrangement of the components in a typical gamma camera. The boxes labelled S can represent a range of different components, depending on the crystal type and the techniques employed. For scintillation crystals, the boxes would typically represent individual photomultiplier (PM) tubes or solid-state-based silicon counterparts, but they can also represent individual sections in a position-sensitive PM tube or pixels on a charge-coupled device (Anger, 1958; Peterson and Furenlid, 2011). For semiconductor-based cameras, the boxes represent individual electrodes and the asso-

ciated readout-electronics (Peterson and Furenlid, 2011).
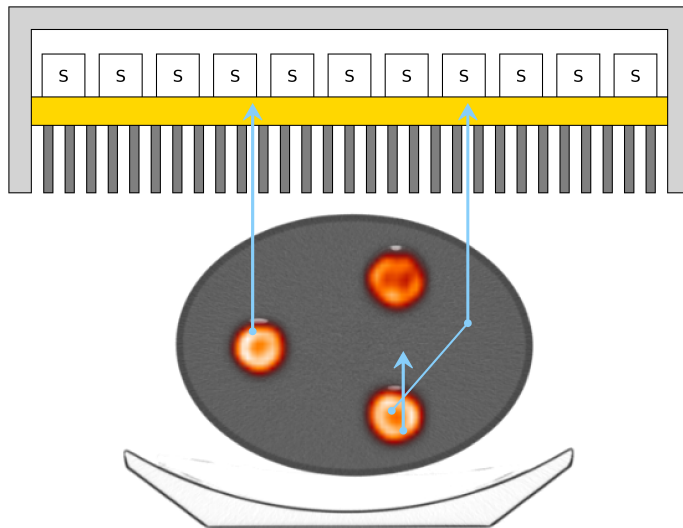
Figure 2.1: Example of a typical gamma camera assembly with an illustration of an image acquisition process. The camera assembly is shown at the top. The detector crystal is shown in yellow, the collimator in grey and the assembly casing in light grey. The white boxes labelled S represent the sensors and readout-electronics. An artificial object imaged by the camera is shown underneath as a SPECT/CT fusion image, depicting three spherical sources in a water-filled elliptical container. The blue arrows depict the tracks of the photons emitted.

The radiopharmaceutical administered emits radiation isotropically. Hence, measuring the distribution of photon interactions in the crystal does not, on its own, convey useful information about the spatial distribution of the radiopharmaceutical. Therefore, gamma cameras employ collimators to restrict the directions or positions that incident photons are permitted to have if they are to pass through and hit the crystal. Through this restriction, the origin of a detected photon can be inferred from the interaction position in the crystal, allowing the camera to form meaningful images of the source distribution. Figure 2.1 illustrates the role of the collimator. In this implementation, a parallel-hole collimator is shown, which only allows photons travelling upwards within a limited angle of acceptance to hit the camera crystal. Hence, the images produced by the camera will resemble the distribution of activity integrated over all source depths. Other collimator designs are also possible, another prominent type being the pinhole collimator. Such collimators may introduce distortions or depth-dependent magnifications, but the images acquired are still usable for visual interpretation or tomographic reconstruction, as the collimator enforces a relationship between the positions in the image and the possible photon origins.

Even with a collimator, not all of the photons detected convey useful information. Figure 2.1 depicts one ideal photon track that traces directly from the emission point to the camera, and one track, whereby the photon scatters before reaching the camera. The scattered

photon gives a false impression in the image acquired that activity exists underneath its final point of interaction. Such events can be excluded from the camera image by studying the energy spectrum of the incident photons; as Compton scattering decreases a photon's energy, gamma camera images are typically only formed by accepting events, the estimated energies of which are within a set energy range (energy window) set over one of the characteristic emission energies of the imaged radionuclide.

1.1 Image-degrading processes

Ideally, the images acquired by gamma cameras would accurately represent the relative distribution of a radiation source. However, due to a number of distinct events possible in the photon transport such an assumption would not be completely accurate. These events can be considered to cause image-degrading effects, which can be defined as anything that causes the acquired image to differ from an unperturbed projection of the source distribution onto the camera surface. Image-degrading effects are typically divided into a number of separate categories, which should be taken into consideration when interpreting or processing raw camera images. The most important effects are as follows:

- Attenuation. This concept can be defined in the narrow-beam geometry framework, wherein a beam of photons is aimed towards a detector through a material, and any interaction between a photon and the medium causes it to miss the detector. The decrease of photons remaining in the beam as a function of depth in the material is referred to as attenuation, which therefore incorporates not only photoelectric absorption, but also Compton scattering, pair production and elastic scatterings. The end-result of attenuation is that sources with a greater amount of matter in front of the camera will falsely appear to be dimmer in the acquired image.

- Scatter. This concept is related to attenuation, but is often considered separately. Photons that undergo one or more scattering interactions in a material may still hit the camera and contribute to the image formation, depending on the final photon energy and the energy window used. Even with a window over a prominent radionuclide emission, some amount of scatter will be measured, as the energy window must have an appreciable width. The practical width of the energy window is ultimately governed by the non-zero energy resolution of the camera, which in turn is primarily related to the crystal and readout-electronics used. Scatter events cause a degradation of the image quality, as they add additional signal across the image, which does not reflect the actual activity distribution.

- Spatial resolution and partial volume effects. Gamma cameras do not yield perfectly sharp depictions of the objects imaged, mainly due to the working principles and

design constraints of the collimators. Uncertainties in the estimation of the incident photon interaction positions in the crystal can also play a role. The resulting images have a blurriness associated with them, which can normally be modelled as a convolution between the true source distribution and a point-spread function (PSF) (normally a Gaussian function). Spatial resolution in nuclear medicine is often defined or related to the width of the Gaussian, which is often quantified as the full width at half maximum (FWHM). This can be contrasted with some other fields of medical physics, in which spatial resolution and the image pixel size may be synonymous (e.g. computed tomography (CT) or magnetic resonance imaging (MRI)). For gamma cameras, however, the Gaussian FWHM is generally larger than the pixel sizes used.

The spatial resolution of nuclear medicinal images means that the signal in an object and its surrounding background may blur together around the object boundary. I.e. a portion of the signal from an object will appear outside the object's true boundary in an image and a portion of the signal from the background will be registered inside the object boundary. This is called the partial volume effect (PVE), which may affect the accuracy of activity estimations unless corrected for.

- Septum penetration. Collimators allows gamma cameras to generate images of the spatial distribution of activity uptake by absorbing photons that travel towards the camera at unwanted incidence angles or in unwanted positions. The walls of the collimator do, however, have a finite thickness, which means that some unwanted photons will pass through the collimator walls and hit the camera crystal. The amount of penetration will depend on factors, such as the photon energy, the collimator design and the source-collimator distance. Septum penetration will yield additional signal over the acquired image, worsening the image quality. The effect can be alleviated by using a collimator appropriate for the photon energies and energy window involved, with thicker collimator walls being advisable for higher photon energies.

2 Anger cameras

Most gamma cameras in use today are based on the original design of Anger (1958), illustrated in Figure 2.2. The design is a scintillator-type detector, the defining mode of operation of which for detecting photons and quantifying photon energy is to convert the energy deposited into flashes of light. Most designs employ thallium-doped sodium-iodide (NaI(Tl)) crystals to detect the impinging photons. To determine a photon's two-dimensional point of interaction in the crystal, an array of PM tubes is employed. When a photon interacts with the crystal, the small flash of light produced by the scintillator crystal will be collected by several PM-tubes, which convert the scintillation light into measurable electrical signals. The total signal produced by all of the tubes will be proportional to the

energy deposited. The interaction point can be determined by averaging the positions of all of the PM-tubes, weighted by their respective measured signals.
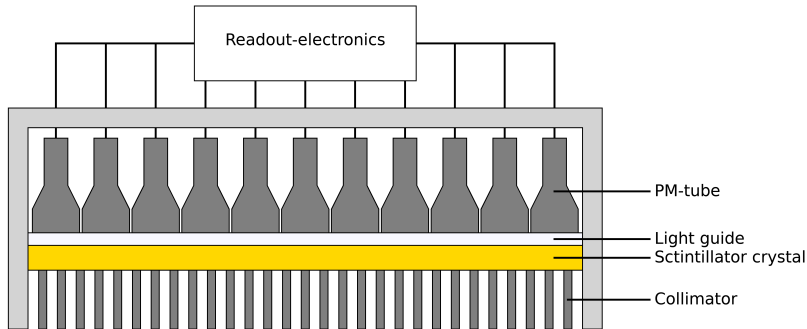
Figure 2.2: Cross-sectional drawing of an Anger camera.

3 Semiconductor detectors

A general drawback of scintillator-based radiation detectors is their relatively poor energy resolution. This property stems from inefficiencies in the process, where the energy deposited by an ionising particle in the detector gets converted to electrical signals. This process of converting the deposited energy into scintillation light and then converting this light into electrons is relatively inefficient and the number of electrons that enters the PM-tubes is, therefore, relatively small. These electrons can be described as information-carriers and the number of electrons generated will determine the estimated energy deposited in the detector. Due to the small number of information carriers, the statistical variations in the number of carriers created by an interaction in the detector will be high and this variation translates into a variation in the estimated energy deposition in the detector. A low average number of information carriers created per amount of energy deposited, therefore, causes poor energy resolution in a detector.

Semiconductor-based detectors can serve as an alternative to scintillators, when better energy resolution is desired. This detector type generally has a higher energy resolution, owing to lower number of steps in the generation of a signal from the energy deposited and a generally lower average amount of energy required to form information carriers.

An example drawing of a semiconductor detector is shown in figure 2.3. The detector consists of a semiconductor crystal, an anode and a cathode. The illustration in figure 2.3 shows a pair of wide anode and cathode plates attached to a semiconductor (of thickness d), but other crystal and electrode configurations are possible. A potential V is applied over the electrodes, strengthening the electric field across the detector volume. In the semiconductor

9

crystal, the energy states of the electrons are restricted to two possible energy bands. The two bands are labelled as the valence band (lower band) and the conduction band (upper band) and a gap separates the two bands. Electrons in the valence band have their motion limited to certain points in the crystal, whereas electrons in the conduction band may move more freely within the crystal. When an ionising particle interacts with the crystal, the deposited energy causes valence electrons to transition to higher energy states in the conduction band and the electric field over the crystal causes these electrons to move towards the anode. The vacancy in the valence band left by the electrons will constitute a positive charge in the crystal. Such vacancies are called holes and may move across the crystal in a manner analogous to that of positively charged particles under the influence of an electric field.

When an ionising particle interacts with the detector, the energy deposited will elevate electrons to the conduction band, thus creating electron-hole pairs. The electric field applied will cause the electrons and holes to drift towards the anode and cathode respectively. These motions will give rise to measurable currents in the electrodes and an integration of these currents over time can yield an induced charge (time-integrated current) proportional to the energy deposited.
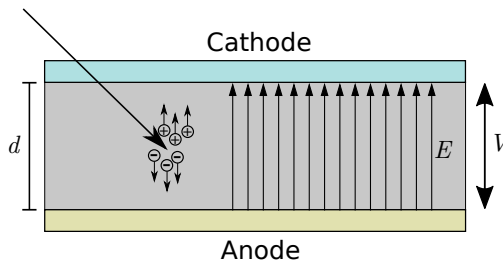
Figure 2.3: Illustration of a cross-section of a semiconductor detector.

When moving towards the electrodes, the charge carriers will interact with the semiconductor crystal, which limits the average velocity. The velocity $\vec{v}$ of a charge carrier will be given by

$$\vec{v} = \mu \cdot \vec{E}, \tag{2.1}$$

where μ is the carrier mobility (unit $\mathrm{m^2\,V^{-1}\,s^{-1}}$) and $\vec{E}$ is the electric field (unit $\mathrm{V\,m^{-1}}$) (Knoll, 2010). Electrons and holes will generally have different mobilities, denoted by μ_e and μ_h respectively, which are unique properties for each semiconductor material.

Additionally, every semiconductor crystal produced will generally contain some impurities and defects. The effect of these is that electrons and holes moving through the crystal may become trapped at such defect sites. The end result of this trapping is a gradual reduction in electron and hole charge densities travelling towards the electrodes over time, which reduces the currents induced in the electrodes and the final induced charge. Trapping is quantified as average electron τ_e and hole τ_h lifetimes (unit s), which are also properties of

the semiconductor material. If one assumes a constant electric field over the crystal, then an average range λ_x (unit m), where the subscript x can denote e or h, is given by

$$\lambda_x = \mu_x \cdot \tau_x \cdot E = \mu_x \cdot \tau_x \cdot V/d, \tag{2.2}$$

where the approximation $E = V/d$ has been made for the geometry in Figure 2.3 (Guerra et al., 2008).

Trapping occurs in all semiconductor materials, but should not have a noticeable impact on the energy spectrum of the device, as long as the average range of the electrons and holes are long compared to the dimensions of the crystal. This is generally the case for silicon and germanium (Table 2.1), which are the two most commonly used semiconductor detector materials. These materials do, however, have some drawbacks, such as low absorption of higher-energy photons due to a lower atomic number (Si) and cooling requirements (Ge).

Table 2.1: Typical properties for semiconductors. Adapted from McGregor and Hermon (1997) and Knoll (2010).

Material	Atomic number	Density [g cm^{-3}]	Mobility [cm^2 V^{-1} s^{-1}] Electrons	Holes	Lifetime [s] Electrons	Holes
Si	14	2.33	1450	450	1×10^{-4}	1×10^{-4}
Ge	32	5.33	36 000	42 000	1×10^{-4}	1×10^{-4}
HgI$_2$	80|53	6.4	100	4	7×10^{-6}	3×10^{-6}
GaAs	31|33	5.32	8000	400	1×10^{-8}	1×10^{-8}
CdTe	48|52	6.06	1000	80	1×10^{-6}	1×10^{-6}
Cd$_{0.8}$Zn$_{0.2}$Te	48|30|52	$\sim$6	1350	120	1×10^{-6}	2×10^{-7}

3.1   Cadmium zinc telluride (CZT)

An ideal semiconductor detector would have a large sensitive volume, good charge transportation properties (high mobility and low trapping for holes and electrons), a high atomic number (for high absorption of high-energy photons) and would operate at room temperature (Knoll, 2010). Germanium and silicon detectors are commonly used, as their favourable charge transportation properties (high mobilities and long lifetimes) allow for large detector sizes, but they have the drawbacks of having relatively low atomic numbers and may require cooling. To create a detector which avoids these drawbacks, other semiconductor materials should be used. This generally involves using a compound semiconductor material, i.e. a material which consists of two or more different elements. Compound semiconductors encompass a wide range of materials with a correspondingly large range of material properties. Compounds exist, which offer larger band gaps, allowing them to be operated at room temperature, for example, as well as higher atomic numbers. Many compounds can also be blended together, which allows further optimisation and tailoring of a material for certain applications. Compound semiconductor crystals are, however, generally more difficult to grow compared to silicon and germanium and, as a result, have poorer charge

transport properties. Few compound semiconductors have, therefore, been developed sufficiently to be implemented in detector systems. Examples of more commonly used materials are CdTe, HgI_2, GaAs and $Cd_{1-x}Zn_xTe$ (McGregor and Hermon, 1997; Owens and Peacock, 2004; Knoll, 2010). Typical properties are given in Table 2.1.

CdTe and $Cd_{1-x}Zn_xTe$ (cadmium zinc telluride (CZT)) are the most well researched semiconductors for nuclear medicine (Peterson and Furenlid, 2011). CZT consists of a blend of CdTe and ZnTe, with x typically in the range of 4 % to 20 %, and has been found to have favourable properties compared to CdTe. Several systems that are based on CZT are commercially available, e.g. Discovery NM/CT 570c (GE Healthcare), D-SPECT (Spectrum Dynamics) and CrystalCam (Crystal Photonics) (Peterson and Furenlid, 2011; Knoll et al., 2015; Pretorius et al., 2015).

CZT does, however, have poor charge transportation properties, which is common for compound semiconductors. The mobility and lifetime for holes are particularly short, which affects the spectroscopic capabilities of CZT-detectors for any reasonably thick crystals. Parallel-plate configurations (Figure 2.3) are particularly impacted by this, but there are ways to mitigate the effects and regain sufficient spectroscopic performance. One approach is to use more detailed analysis and processing methods on the signal pulses from the detector (e.g. study both pulse height and rise time) to estimate the depth of interaction and discard or compensate for events that suffer more from trapping (Verger et al., 1997; Knoll, 2010). The other approach involves the use electrode configurations, where the detector pulses are more sensitive to one of the charge carrier types (Barrett et al., 1995; He, 1995; Owens and Peacock, 2004). Common configurations include coplanar grids and pixelated electrodes. The latter type (illustrated in Figure 2.4) is typically used in CZT-based gamma cameras (Peterson and Furenlid, 2011; Knoll et al., 2015; Pretorius et al., 2015) as image formation is rather straightforward and will be described in more detail in sections 3.2 and 3.3.

3.2 Charge transport and signal induction

To understand the consequences of charge trapping and the effect of different electrode configurations, it is necessary to understand the processes involved in the formation of a detector signal pulse. For a simple geometry, such as the parallel-plate configuration, the detector pulses can be determined through a conservation-of-energy argument (Knoll, 2010), but for arbitrary configurations the Shockley-Ramo theorem can be used (Shockley, 1938; Ramo, 1939). The theorem considers a detector volume with a number of separate electrodes attached and states that a charge q at position $\vec{r}$ moving at a velocity $\vec{v}$ induces a current i on one of the electrodes (numbered k) according to

$$i = q \cdot \vec{v} \cdot \vec{E}_k(\vec{r}), \tag{2.3}$$
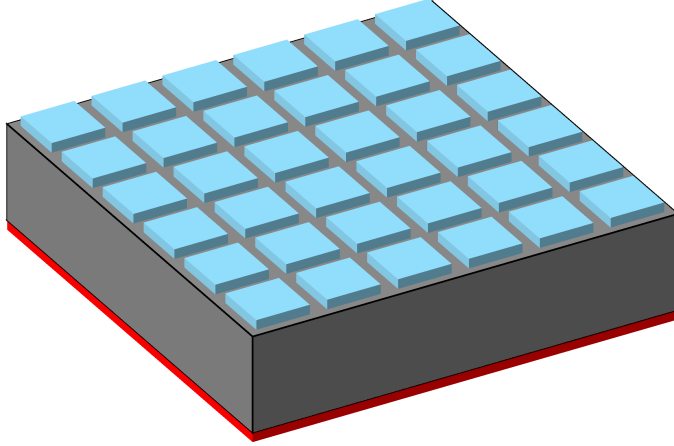
Figure 2.4: Illustration of a pixelated semiconductor detector. The semiconductor crystal is shown in grey, the cathode in red and the anode contact pads in blue.

where $\vec{E}_k\,(\vec{r})$ is the so-called weighting-field (associated with electrode k). The charge velocity $\vec{v}$ is linked to the electric field $\vec{E}$ of the detector by equation 2.1. The electric field $\vec{E}$ is the gradient of the detector's electric potential φ (unit V)

$$\vec{E} = -\nabla\varphi, \tag{2.4}$$

which can be obtained by solving Gauss´s law

$$\nabla^2\varphi = \frac{\rho}{\varepsilon}, \tag{2.5}$$

where ρ is the charge density in the detector volume and ε is the permittivity of the detector material (Knoll, 2010; Myronakis and Darambara, 2011). For equation 2.5, boundary conditions must be applied at the edges of the detector volume. These conditions are typically that certain external voltages are applied at the attached electrodes (e.g. –600 V for cathodes and 0 V for anodes).

The weighting-field $\vec{E}_k$ is similarly related to a weighting potential weighting potential φ_k (unitless) via

$$\vec{E}_k = -\nabla\varphi_k. \tag{2.6}$$

The weighting potential φ_k is, by definition, determined similarly to φ, but with the space charge ρ ignored (set to zero), using the equation

$$\nabla^2\varphi_k = 0. \tag{2.7}$$

As an additional part of the definition of the weighting potential, equation 2.7 is solved with the boundary conditions that electrode k is held at unit potential and all other electrodes are held at zero.

It should be noted that the electric field $\vec{E}$ and potential φ are 'global' properties of the detector and correspond to real physical fields that influence charges in the detector. The weighting field $\vec{E}_k$ and potential φ_k, on the other hand, are only properties of one electrode and do not correspond to any real fields. Rather, they are tools used to calculate the signal pulses produced by the electrode k (using equation 2.3).

The signal pulse seen by a detector's readout-electronics corresponds to the total induced charge ΔQ, given by the time-integration of the induced current i

$$\Delta Q(t) = \int_0^t i(t') \, \mathrm{d}t'. \tag{2.8}$$

An alternative, potentially more intuitive, formulation of equation 2.3 is as follows.

$$\Delta Q = q \cdot \Delta \varphi_k = q \cdot \left(\varphi_k(\vec{r}_{\mathrm{end}}) - \varphi_k(\vec{r}_{\mathrm{start}}) \right), \tag{2.9}$$

which states that a charge carrier moving between two positions ($\vec{r}_{\mathrm{start}}$ and $\vec{r}_{\mathrm{end}}$) in a detector volume will induce a charge equal to its charge q multiplied by the difference in the weighting potential between the two positions.

An important fact shown by the Shockley-Ramo theorem is that a signal pulse from the detector is gradually built up as the charge carriers move across the detector volume. This is in contrast to the naive (and incorrect) notion that the detector signal is formed at the moment when a charge carrier touches an electrode. Such a notion is incorrect, as it expects the signal pulse to form instantaneously and does not allow for a charge carrier to contribute to the signal if it becomes trapped. On the contrary, equation 2.3 shows that a signal will be generated whenever charge carrier moves up or down along a gradient of a weighting potential. Equation 2.9 subsequently shows that a net signal will be generated as long as the weighting potential has different values at the start and end point.

Figure 2.5 demonstrates the weighting potential of an anode in a parallel-plate configuration and in a pixelated configuration, respectively. For the parallel-plate configuration, the weighting potential decreases linearly from 1 to 0 between the anode and the cathode. Consequently, the associated weighting field is uniform and a moving charge will induce the same current in the anode regardless of its location within the detector (equation 2.3). In other words, this configuration has a uniform 'sensitivity' over the whole detector volume. In contrast, the weighting potential for a single anode in a pixelated configuration shows a steep gradient within a limited region near the anode surface. Consequently, the anode is very sensitive to the movement of charge within this region and quite insensitive throughout the rest of the detector volume. As a rule of thumb, a moving charge will not induce much current in an anode unless it is within a distance from the anode equal to the anode's width (Barrett et al., 1995).
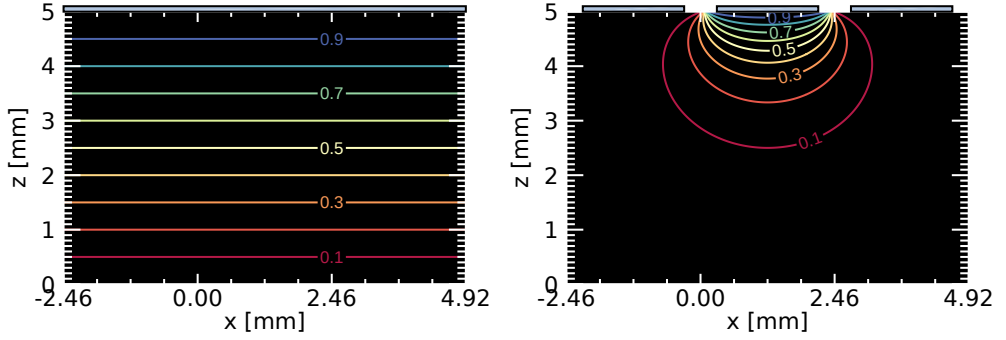
Figure 2.5: Contour plots of weighting potential cross-sections (for anodes) for two different electrode configurations. Anodes are drawn at the top of each image (grey rectangles). A cathode (not shown) covers the entire bottom in both cases. The left image shows the weighting potential for the anode in a parallel-plate configuration (Figure 2.3). The right image shows the weighting potential for one of the anodes in a pixelated configuration (Figure 2.4).

Equations 2.1, 2.3 and 2.8 provide a method for calculating signal pulses, but this method is only valid for point charges. More generally, groups of charges tend to spread out into clouds due to diffusion, which may affect the induced signal. To describe the motions of charge clouds, it is necessary to introduce the distributions $n\,(\vec{r}, t)$ (electrons) and $p\,(\vec{r}, t)$ (holes). The evolution of these distributions over time are described by standard drift-diffusion equation (Prettyman, 1999; Mathy et al., 2004; Myronakis and Darambara, 2011)

$$\frac{\partial n}{\partial t} = -\nabla \cdot (\mu_n n \nabla \varphi) + \nabla \cdot (D_n \nabla n) + G_n - R_n, \tag{2.10}$$

$$\frac{\partial p}{\partial t} = \nabla \cdot (\mu_p p \nabla \varphi) + \nabla \cdot (D_p \nabla p) + G_p - R_p. \tag{2.11}$$

The $\nabla \cdot (\mu_x x \nabla \varphi)$ term, where x denotes n or p, is the counterpart to equation 2.1 and describes the charge cloud moving along the electric field. The $\nabla \cdot (D_x \nabla x)$ term, where D_x is a diffusion constant, describes the dispersion of the cloud due to diffusion. The creation of new charges and trapping of existing charge is described by the the terms G_x and R_x, respectively. The rate of charge trapping is proportional to the amount of existing charge and is given by $R_x = x/\tau_x$, where τ_x is the mean lifetime of the charge carrier. Equations 2.10 and 2.11 are initial-value problems, and the state of the charge clouds are typically $x\,(\vec{r}, t) = 0$ until excess charges are generated. Excess charge created by the interaction of ionising radiation at a position $\vec{r}_0$ at the time $t = 0$ can be described by $G_x = q \cdot \delta\,(|\vec{r} - \vec{r}_0|) \cdot \delta(t)$.

The diffusion constant D_x is given by the Einstein relation $D_x = \frac{k_B \cdot T}{q} \cdot \mu_x$, where k_B is the Boltzmann constant, T is the absolute temperature of the detector and q is the charge of the particles involved (Einstein, 1905).

Solving equation 2.10 or 2.11 gives a full time-dependent charge cloud. Given such a cloud,

the charge induced on electrode k can be calculated as

$$\Delta Q_{x,k}(t) = \int_0^t \int_{\vec{r} \in \Omega} q \cdot x\left(\vec{r}, t\right) \cdot \mu_x \cdot \nabla\varphi\left(\vec{r}\right) \cdot \nabla\varphi_k\left(\vec{r}\right) \mathrm{d}\Omega\, \mathrm{d}t', \qquad (2.12)$$

where Ω is the detector volume (Prettyman, 1999; Mathy et al., 2004; Guerra et al., 2008; Myronakis and Darambara, 2011).

Figures 2.6 and 2.7 illustrate the evolution of an electron cloud and the signal pulse it induces in an anode for a parallel-plate and a pixelated configuration, respectively. In both cases, a uniform electric field is applied (0 V at the anode-side and –600 V at the cathode-side) and a point-like charge cloud has been initiated near the cathode ($z \simeq 0.5$ mm) at $t = 0$. A mobility and lifetime typical for electrons in CZT have been used, but the diffusion coefficient has been increased for illustrative purposes. For the parallel-plate configuration, the signal increases linearly as the electron cloud travels though the detector volume and levels off once the electrons leave the detector. For the pixelated configuration, the signal rises slowly at first until the cloud comes within a short distance of the anode, after which the signal increases quickly as the cloud traverses the steep gradient of the weighting potential.
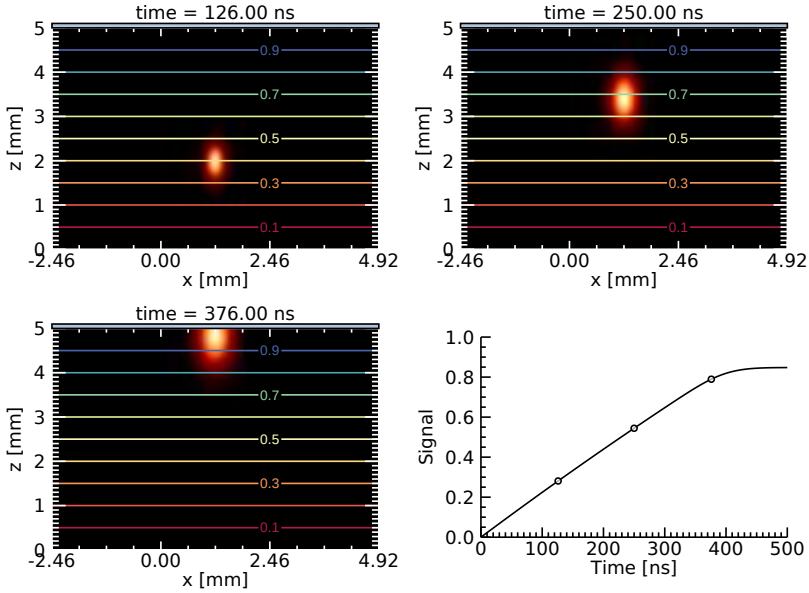

Figure 2.6: Illustration of an electron cloud moving though a detector volume (parallel-plate configuration), along with the signal ($\Delta Q(t)$) induced in the anode. The charge cloud is shown with a red-white colour table and the weighting potential is overlaid as a contour plot. The time-points at which the charge cloud is shown are marked by circles on the signal curve.
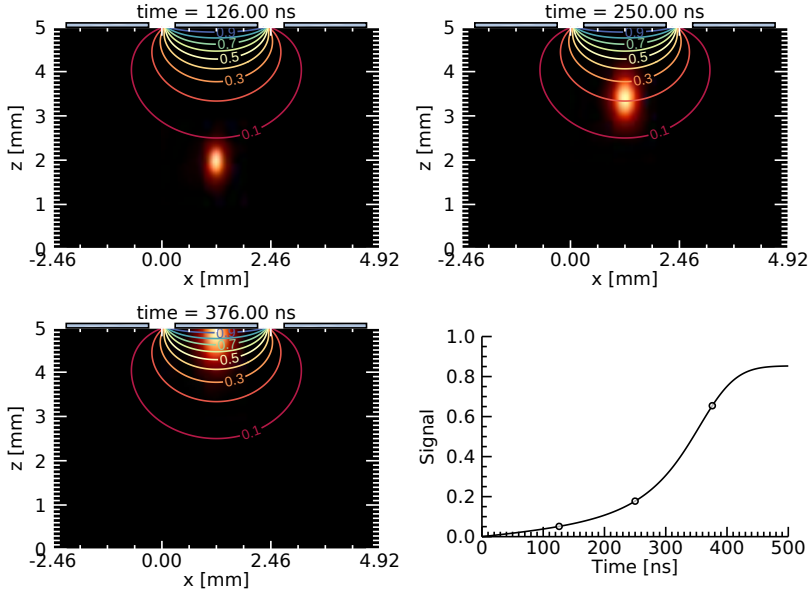
Figure 2.7: Illustration of an electron cloud moving though a detector volume (pixelated configuration), along with the signal ($\Delta Q(t)$) induced in the middle anode. The charge cloud is shown with a red-white colour table and the weighting potential is overlaid as a contour plot. The time-points at which the charge cloud is shown are marked by circles on the signal curve.

3.3   Consequences of incomplete charge induction

Equations 2.10–2.12 provides a method for determining the response of an electrode to a single radiation interaction, generating a total charge q at a point $\vec{r}_0$. Given this method, it can be practical to map out a normalised response for every possible interaction position $\vec{r}_0$. For this task, the induced charge given by equation 2.12 is considered to be a function of both t and $\vec{r}_0$, i.e. $\Delta Q_{x,k}(t) = \Delta Q_{x,k}(\vec{r}_0, t)$. The normalised response map is called the charge induction efficiency (CIE) and is defined as $\eta_{x,k}(\vec{r}_0, t) = Q_{x,k}(\vec{r}_0, t)/|q|$. Calculating the CIE for a large set of starting positions (e.g. on a 100 × 100 × 100 three-dimensional grid) via equations 2.10–2.12 is computationally expensive and there is a more efficient method based on alternative equations (described in Appendix A). Figures 2.8 and 2.9 show CIE maps for the anode in a parallel-plate configuration and for one anode in a pixelated configuration. Both maps have been determined using settings and properties typical for CZT, and include signal contributions from electrons only. The omission of holes is motivated by their low mobility and short lifetime, resulting in a limited signal contribution. For the parallel-plate configuration, the signal induction behaviour demonstrated in Figure 2.6 (uniform sensitivity to charge motion throughout the detector volume) means that the total induced charge will depend heavily on the interaction depth. For the pixelated configuration, the behaviour where most of the signal is induced within a limited region near the anode (Figure 2.7) results in a plateau in the CIE maps, where a similar

total induced charge is obtained for interaction depths of between approximately 0 mm and 3.5 mm. Consequently, the pixelated configuration can be said to be primarily sensitive to the motion of electrons (and insensitive to the lack of motion by holes), and the configuration is hence sometimes referred to as being single polarity sensitive (He, 2001; Guerra et al., 2008). Generally, the degree with which an electrode is sensitive to only one charge carrier type is governed by its width relative to the crystal thickness, with wide electrodes being sensitive to the motions of both charge carriers and smaller electrodes mainly sensitive to only one type of charge carrier (Barrett et al., 1995; Knoll, 2010).

Figure 2.8: Left: Cross-section of a CIE map at a fixed time-point for the anode in a parallel-plate configuration. Right: Signal pulses for different interaction depths. The selected interaction points are indicated by circles on the CIE map.
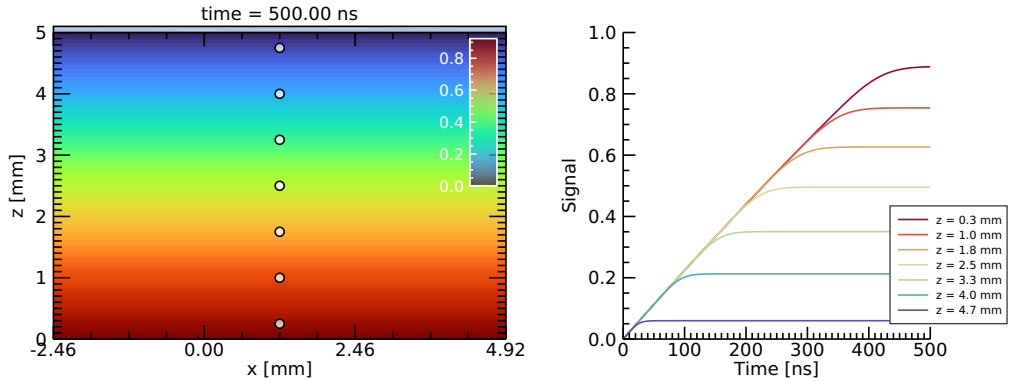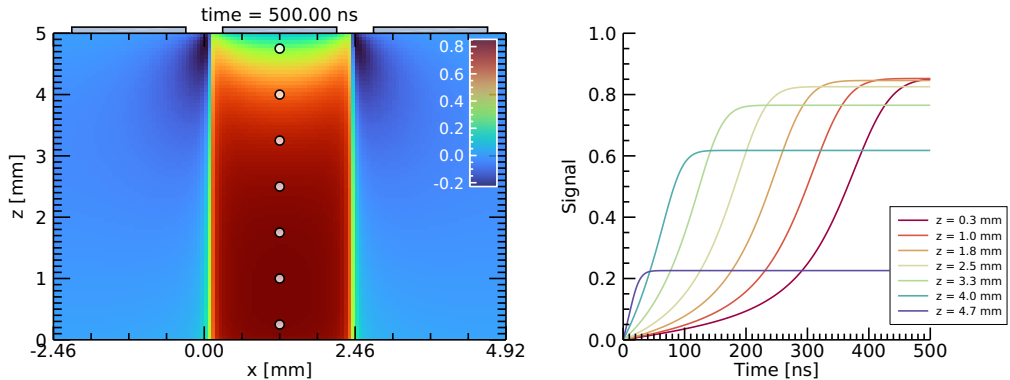

Figure 2.9: Left: Cross-section of a CIE map at a fixed time-point for the middle anode in a pixelated configuration. Right: Signal pulses for different interaction depths. The selected interaction points are indicated by circles on the CIE map.

For a typical pulse-integration circuit in a simple detector, only the final integrated current on the anode is measured and digitised with a multichannel analyser (MCA), with no other signal characteristics taken into consideration. In such a set-up, a photon interacting in the detector (energy depositions E_i at positions $\vec{r}_i$) would contribute a count in an energy bin B proportional to the sum of the resulting signals from each interaction i. I.e.

$$B \propto \sum_i E_i \cdot \eta_k(\vec{r}_i), \tag{2.13}$$

where $\eta_k(\vec{r})$ represents $\eta_k(\vec{r}, t)$ evaluated at a large (or infinite) value for t. As incident photons will interact at random depths in the detector, this means that the same total deposited energy can be scored across a wide range of channel numbers in a spectrum, governed by the CIE value at the points of interaction. Slopes in the CIE map distribute counts across a range of channels, leading to 'tails' of low amplitudes. To obtain a meaningful photopeak, it is necessary to have a plateau in the CIE map, as such a region maps events with the same total deposited energy to the same channel number.

Figure 2.10 presents CIE maps for a parallel-plate configuration (based on Figure 2.8) and a pixelated configuration (the same as in Figure 2.9) and the resulting energy spectra for a set of monoenergetic energy depositions homogeneously distributed throughout the detector depth. Signal contribution from holes has been included for the parallel-plate configuration, as this produced a thin region near the cathode with constant CIE-value. The strong depth-dependence means that a large portion of the events have been counted in a low-energy tail stretching from channel number 900 and downwards. The thin plateau near the cathode assigns events to roughly the same channel number, resulting in a small photopeak at channel 1000. For the pixelated configuration, the larger plateau means that more counts are placed in the photopeak. A low-energy tail remains, owing to the small remaining depth-dependence and the lateral edges of the CIE map.

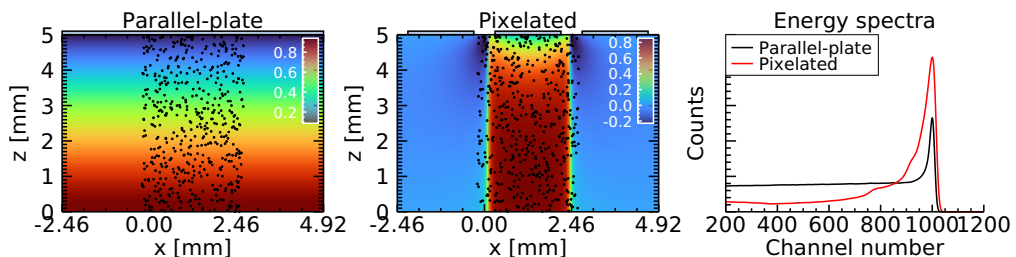**Figure 2.10:** CIE maps with photon interactions and resulting energy spectra. Photon interaction positions are shown with black dots.

It should be noted that Figure 2.10 shows spectra for a worst-case scenario, where a comparatively thick CZT crystal is used together with the simplest possible readout-electronics and radiation interactions are distributed uniformly throughout the detector depth. There

are methods and mechanisms by which the spectroscopic performance of the detector can be improved. More realistically, the spatial distribution of radiation interactions decreases with increasing depths in the detector and spectroscopic performance can, thus, be regained if irradiation takes place from the cathode-side, especially for measurements of low-energy photons. Spectroscopic performance can also be improved with more sophisticated readout-electronics. For instance, by also measuring the total pulse rise time in a parallel-plate detector (note the signal curves in Figure 2.8), one obtains an indirect measure of the depth of interaction. The information obtained is typically presented as bi-parametric spectra with total counts as a function of both final pulse height and pulse rise time, and improved conventional spectra can be obtained by using the rise time to discard or correct events suffering more from trapping (Verger et al., 1997). Similar schemes can also be applied to pixelated detectors, although the depth of interaction can then be inferred by studying the pulse heights or onset delays between the anode and cathode (Knoll, 2010). Sophisticated readout-schemes may be more relevant for parallel-plate detectors, as only having two electrodes makes the implementation simpler and the greater depth-dependence makes the scheme more necessary. In contrast, sophisticated readout-schemes could be difficult to implement in pixelated detectors, as all of the anode pads must be read out individually using hundreds of separate pulse-processing units, usually implemented in a purpose-built application-specific integrated circuits (ASICs). Given the reduced depth-dependence, the need for sophisticated pulse-analysis schemes in pixelated detectors is less pressing.

3.4 New challenges compared to Anger cameras

Manufactured CZT ingots are typically inhomogeneous regarding defects, purity and properties such as charge mobility and lifetime (James et al., 1998). Good crystal parts are typically identified and cut out and detector crystals are assembled from multiple pieces (Knoll, 2010). Each anode pad in a pixelated detector is read out separately with its own dedicated pulse-processing unit, typically incorporated into an ASIC. As the crystal properties beneath each anode pad may differ and, possibly, because each pad has its own pulse-processor, each anode pad produces a unique spectrum with its own energy calibration and energy resolution. Some sections of the detector may not produce a usable spectrum at all due to defective, noisy or dead pixels, potentially owing to defects in the crystal or readout-electronics (Fiederle et al., 2003; Zhang and He, 2004; Zhang et al., 2011; NEMA, 2013). For a given radionuclide and energy window, a CZT-based gamma camera can, therefore, present marked variations in sensitivity between neighbouring pixels. This can be corrected for by using uniformity maps, but the non-uniform energy resolution may still have implications for post-processing techniques, such as scatter correction, as the camera system may not be translation-invariant to the same degree as conventional scintillation cameras. Additionally, the use of a parallel-hole collimator may affect the energy spectra of the pixels as the collimator walls prevents certain regions of each pixel's CIE map from being irra-

diated, meaning that the uniformity correction should potentially be radionuclide- and collimator-dependent (Sandstrom et al., 2019; Roth et al., 2020).

Figure 2.11 presents the performance for individual anode elements in a CZT-based gamma camera. Example spectra for one good, one average and two bad anode elements are shown for a measurement of ^{177}Lu. The surface plot shows the energy resolution of all of the anode elements throughout the camera for the 208 keV peak, determined according to NEMA (2013). Four anodes along the image border and six in the centre have noticeably poorer energy resolutions. The variation in spectral response is also reflected to some degree in the uniformity of acquired images.
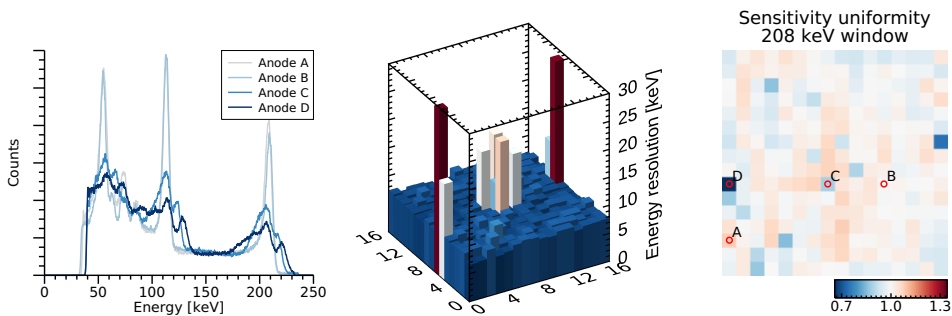
Figure 2.11: Characteristics of individual anodes in a CZT-based gamma camera (16 × 16 anodes). Left: Energy spectra (^{177}Lu) for four selected anodes. Middle: Surface plot of energy resolutions (at 208 keV) for each anode. Right: Image uniformity for a 208 keV energy window. Values above and below 1.0 represent higher and lower sensitivities than the camera-average, respectively. The anode elements for which spectra are shown are indicated with circles and letters.

The energy-tailing present in the spectra have implications for any measurements or image-processing method that aims to isolate and quantify different components contributing to obtained spectra. A common image-processing method that will be affected is scatter-correction, which attempts to isolate scattered and unscattered photons that have been detected within a given energy window (more on this in Chapter 3). For scatter correction that uses multiple energy windows to estimate the amount of scatter, the energy-tailing presents a complicating factor, as primary unscattered photons will be counted not only in their associated photopeak window, but also in any lower windows. A proper window-based correction method must, therefore, account for and model this tailing behaviour, adding complexity to methods that are more straightforward to apply on Anger cameras. Other areas that are affected by the tailing include the measurement of radionuclides with multiple prominent emissions or when two radionuclides are measured simultaneously (Roth et al., 2020; Kacperski et al., 2011). For multi-peak radionuclides, the tailing means that any image-degrading effects that are prevalent for a higher-energy emission (e.g. septal penetration) will affect any image acquired from an energy window set on this emission energy or at any lower energies (Roth et al., 2020). For dual-radioisotope acquisitions (e.g. ^{99m}Tc+^{201}Tl and ^{99m}Tc+^{123}I) whereby the uptake is determined for two radio-

pharmaceuticals from a single common measurement, the tailing presents similar issues as for scatter correction, where emissions from one radionuclide will interfere with the estimated uptake of the other radionuclide (Kacperski et al., 2011; Holstensson et al., 2015; Fan et al., 2015; Takeuchi et al., 2016; Blaire et al., 2016).

4   Small and hand-held gamma cameras

Some areas of nuclear medicine present a need for high-resolution imaging of a limited area. For such examinations, a typical, general-purpose gamma camera with a large field of view (FOV) may be insufficient due to a limited spatial resolution and limited detector orientations (Peterson and Furenlid, 2011). These requirements have led to the development of specialised hand-held gamma cameras, which sacrifice a large FOV in favour of better spatial resolution and a compactness and portability that allow them to be freely oriented and placed close to the object of interest. Figure 2.12 illustrates one such camera (CrystalCam, Crystal Photonics GmbH, Berlin, Germany). A common application for such small hand-held gamma cameras is pre- and intra-operative sentinel lymph node detection in breast cancer patients (Kerrou et al., 2011; Peterson and Furenlid, 2011). Other applications include scintimammography and parathyroid imaging (Kerrou et al., 2011; Heller and Zanzonico, 2011).

Figure 2.12: Illustration of a CZT-based hand-held gamma camera (Knoll et al., 2015; Roth et al., 2020). The left end of the device is a parallel-hole collimator with a front area of approximately $4 \times 4\,cm^2$.

These purpose-built detectors generally differ from the conventional NaI(Tl) Anger camera design in some manner in order to achieve compactness or better spatial resolution. Designs may include the use of position-sensitive PM tubes, silicon-based PMs, arrays of scintillator crystal blocks as opposed to a single continuous crystal block or the use of semiconductor detectors (Popovic et al., 2014; Scopinaro et al., 2008; Eisen et al., 2002; Heller and Zan-

zonico, 2011; Olcott et al., 2007; Abe et al., 2003; Siman and Cheenu Kappadath, 2012; Ortega et al., 2007; Kerrou et al., 2011; Knoll et al., 2015).

The portability that these camera systems offer means that they could easily be used outside of a surgical or nuclear-medicinal department, such as in patient rooms. The small FOV also reduces the need for the patient to remain immobile during the image acquisition. These advantages could make hand-held cameras applicable for more conventional areas of nuclear medicine (i.e. outside the cameras intended niche areas), such as for the determination of biokinetic curves of radiopharmaceuticals. One such field that may benefit is dosimetry in radionuclide therapies, where a hand-held camera could facilitate denser samples over time for image-based dosimetry or pharmacokinetic modelling.

4.1 Hand-held gamma camera used in this thesis

Three papers in this thesis (Paper II, Paper III and Paper V) involves a hand-held and its application to ^{177}Lu imaging and activity quantification. The camera is a CrystalCam (depicted in Figure 2.12), which employs a pixelated CZT detector for photon detection and imaging. Power to the camera and its operation is provided by a regular laptop, which makes the system highly mobile and measurements easy to perform. One of several collimators can be attached to the camera, including a low energy high resolution (LEHR), a low energy high sensitivity (LEHS) and a medium energy general purpose (MEGP) collimator. Collimator specifications are provided in Table 2.2. The size of the camera's FOV is 4×4 cm², and the image matrices it produces are 16×16 pixels. Under normal operation, the camera can measure photon energies from 40 keV up to approximately 250 keV, allowing it to produce images with the ^{177}Lu photopeaks at 55 keV, 113 keV and 208 keV.

Table 2.2: Characteristics for the hand-held camera's collimators. All values are given in mm. Table reproduced from Roth et al. (2020) (Paper II).

Name	Hole length	Wall thickness	Hole width	Material	Hole shape
LEHR	22.6	0.23	2.23	Lead	Square
LEHS	11.2	0.42	2.04	Tungsten	Square
MEGP	11.5	0.96	1.50	Lead	Circular

Chapter 3

Image-based activity quantification and dosimetry

1 Activity quantification

Raw images produced by gamma cameras have the unit of counts, indicating the number of incident photons that have been spatially registered to each image pixel. Such images generally reflect the approximate spatial distribution of the activity underneath the camera and the image values themselves are proportional to the absolute amount of activity in the source. The raw images obtained directly from a camera will, however, not be exact depictions of the source distribution, as emitted photons may interact with the surrounding matter before reaching the camera. Regardless of whether the camera images are to be studied visually in a qualitative manner or are meant to be used to obtain quantitative values, it is typically desirable to process the raw images in such a way that the results reflect source distribution as though it was suspended in air or vacuum. Beyond this process, it is valuable or even necessary for many tasks to have images, the values of which correspond to the amount of activity underneath each pixel or within each voxel. For diagnostic studies, absolute activity uptake values in organs or regions can be of value, as this measure (per amount of administered activity) can be compared with typically normal values to identify possible illness. A common measure for this is the standardised uptake value (SUV), which is routinely used in [^{18}F]FDG positron emission tomography (PET) and less frequently in single photon emission computed tomography (SPECT). For pharmacokinetic studies, having quantitative images of the activity distribution is very valuable, as this reflects the exact distribution of the radiopharmaceutical and allows its absolute accretion or throughput to be determined. For RNT dosimetry, activity quantification is an integral step, as the accumulated activity in a region is directly linked to the AD and that the region and its

surroundings receive.

1.1 Image processing

The task in activity quantification is to convert a number of counts in an image to an amount of activity. This can be performed at a region level, producing the total estimated activity for a selected region, or at a pixel level, producing a map representing the source distribution with most or all image-degrading effects negated. The basic principle for both the region- and pixel-based method is to form a model of the photon transport and the camera system, describing the number of counts detected as a function of the source distribution and the source activity with all or major image-degrading processes factored in. Strictly speaking, such a model results in a function which needs to be inverted or an equation system which needs to be solved, and the general problem can thus be described as finding the two- or three-dimensional activity distribution that produced the measured images.

It is sometimes possible to apply correction methods for various image-degrading processes in a pre-processing step. The aim of such methods is to produce images (still measured in counts) that more closely correspond to an ideal projection of the source distribution as though it was suspended in vacuum. If all major image-degrading processes can be corrected in this way (which may be feasible for e.g. conjugate-view systems), then simply applying a measured system sensitivity as a final step may be necessary to obtain a quantitative image of the activity distribution. Such a workflow is easy to follow and it is straightforward to calculate activity values, as long as the information needed by the correction methods can be acquired. However, activities estimated this way may be less accurate than other approaches, as all correction methods will operate on the acquired planar images and will not take the full three-dimensional activity distribution into consideration.

The alternative to pre-processing is to work with source distribution estimates, calculate the associated planar system images using the system model, and therein include selected image-degrading processes. The source distribution estimate would then have to be updated iteratively, for example, by a least-squares or maximum likelihood expectation maximization (ML-EM) method. This approach can be favourable for activity quantification, as the image-degrading processes modelled within a system-model with a three-dimensional activity distribution can potentially be more accurate than the more approximate pre-processing correction methods. This approach also offers an alternative way to account for some degrading processes if insufficient information for a corresponding pre-processing method can be obtained (e.g. unknown source depth for attenuation correction). For iterative tomographic image reconstruction this approach is natural, but planar methods such as the one described in section 1.1.4 can be grouped under this category as well.

1.1.1 Attenuation

Attenuation correction can be performed if the composition (density and mass-attenuation coefficient) of the attenuating material is known, along with the source depth or, in certain cases, the total object thickness.

For planar imaging, conjugate-view acquisition is a common approach that simplifies attenuation correction (Siegel et al., 1999). The basis for this method is the acquisition of two planar projections in opposing directions, and forming the geometric mean of the two images produces an image whose values are approximately independent of the source depth and only depend on the objects attenuation coefficient and total thickness. A map of this quantity can, for example, be acquired using transmission scans with an external radionuclide-source or calculated from a matched CT image, and a complete attenuation correction can be performed afterwards.

For SPECT images reconstructed using iterative approaches (e.g. ML-EM), attenuation can be corrected for by incorporating this aspect of the photon transport into the system model (Dewaraja et al., 2012). As this type of reconstruction attempts to estimate the source distribution that is most likely to have produced the acquired projections under the given system model, incorporating attenuation means that the resulting activity distribution estimates will be free of this image-degrading process. Typically, attenuation or density maps are derived from CT images and incorporated into the system model to accurately account for attenuation.

Conjugate-view and SPECT acquisitions would typically be preferable if attenuation-correction is to be performed and activity quantification is of interest. Attenuation-correction is also possible for individual planar images as long as the source depth and material composition is provided or can be estimated, but camera systems incapable of conjugate-view or tomographic acquisitions may be less likely to be capable of estimating these parameters. Still, there are methods for source depth estimation that do not rely on CT images etc. For example, the ratio of counts within a photopeak and scatter window can be used to estimate depth. Another method is to use an isotope with multiple emission energies and take advantage of the difference in attenuation between the photopeaks to estimate the source depth (Strand and Persson, 1977).

1.1.2 Scatter

Scatter correction methods can typically be described as attempting to estimate the scatter-contribution though either measurements or modelling.

A common measurement-based method is the triple energy window (TEW) method, which

employs a main energy window placed over the photopeak and two additional windows on either side of the main window (Ogawa et al., 1991). The correction method operates on each pixel separately, and the underlying assumption is that the spectrum of scattered photons inside the main energy window can be approximated as a linear function of the photon energy. With this assumption, the number of scattered photons counted in the main energy window can be estimated from the number of counts in the two side-windows, and scatter correction is applied by decrementing the pixel values of the main window image by these estimates. The method is practical, but the scatter subtraction leads to an increase in image noise (Ljungberg et al., 2016).

Model-based approaches employ models of the amount and spatial distribution of the scatter contribution to correct acquired images. One such approach is to assume that the scatter contribution can be described through a convolution with a scatter-point-spread function. Such a response function can be estimated through measurements or Monte Carlo simulations, and scatter correction can be implemented as a deconvolution (Sjögreen Gleisner and Ljungberg, 2012). Such a technique does, however, assume that the scatter function is spatially invariant, meaning that any variability in the scatter response with source depth or effects of an inhomogeneous scattering material cannot be accounted for (Frey and Tsui, 1993). For iterative tomographic reconstruction methods, model-based methods can employ the depth-information provided by the estimated source distribution, possibly augmented with information from a CT image to derive a better estimate of the scatter contribution (Frey and Tsui, 1993; Frey and Tsui, 1996).

It is also possible to model the scatter contribution using a build-up factor, describing the increased number of transmitted photons due to deviations from the narrow-beam geometry assumed by the attenuation correction (Siegel et al., 1999). The build-up factor is a function of the source depth and needs to be experimentally measured under conditions similar to those in which the method is applied (e.g. same radionuclide and collimator and similar geometries and source sizes).

There are also methods that combine aspects from both the measurement-subtraction and modelling approaches. For example, Kacperski et al. (2011) presents a method described as a combination of the TEW method and modelling, employing measurements on several energy windows with a model of the detector and scatter behaviour to correct for scatter and cross-talk dual-radionuclide measurements on a CZT-based gamma camera.

1.1.3 Spatial resolution and partial volume effects

The limited gamma camera spatial resolution can to some degree be negated through methods such as deconvolution (Ogawa et al., 1988) or by including effects of the resolution within the system model in iterative tomographic reconstruction (Pretorius et al., 1998).

However, the camera system generally cannot be reproduced precisely and the estimated source distributions will always contain some amount of blurriness and noise, and attempts at resolution recovery may further introduce image artefacts. Because of this, activities estimated for individual pixels or voxels can have larger deviations from the true value and, in practice, activities are typically estimated as average values for whole regions (Ljungberg and Sjögreen Gleisner, 2011; Gustafsson et al., 2017).

Some degree of limited spatial resolution will always remain in the images and estimated activities, even region-averages, will, therefore, always be affected systematically by PVEs, whereby some level of activity in a region 'spills out' into the surrounding background and some amount of background activity 'spills in'. The effect of the activity misplacement can be quantified using recovery coefficients (RCs), defined as the estimated activity within a region divided by the actual activity in the region. The RC values depend on a number of factors, primarily how large the region is compared to the system resolution FWHM. It is possible to characterise how the RC depends on a number of such factors and employ this characterisation to correct activity estimates for systematic errors through various RC-correction methods. Figure 3.1 shows examples of RC-curves for spherical sources with no background activity (Figure 2.1). Recoveries measured for this source shape and geometry (low background activity) could, for example, be applied to the correction of activities measured in tumours. Recoveries are demonstrated for two SPECT reconstruction settings, one where attenuation and scatter is modelled in the reconstruction and one where the system resolution is also modelled. As can be seen, larger sources have recoveries closer to 100 % as spill-out mainly affects the outermost section of the source. As the outermost shell constitutes a smaller portion of the total source volume in larger sources, this explains the decreasing level of underestimations. Regardless of the reconstruction settings, the activities of hot sources in a cold background will tend to be underestimated, but applying a resolution correction to the images produces recoveries closer to 100 %, as a larger portion of the activity is correctly located within the object boundaries. Generally speaking, the shape of a source and the activity uptake in the surrounding tissues will affect the RC. For such scenarios, there are more comprehensive methods that can estimate the RC by considering the delineated volume, potentially in conjunction with the estimated activity distribution and a model of the camera system (Thomas et al., 2016). For organs, with shapes and surroundings that may be more consistent across different patients and acquisitions, a fixed RC-value may suffice (Gustafsson et al., 2015; Sundlöv et al., 2018).
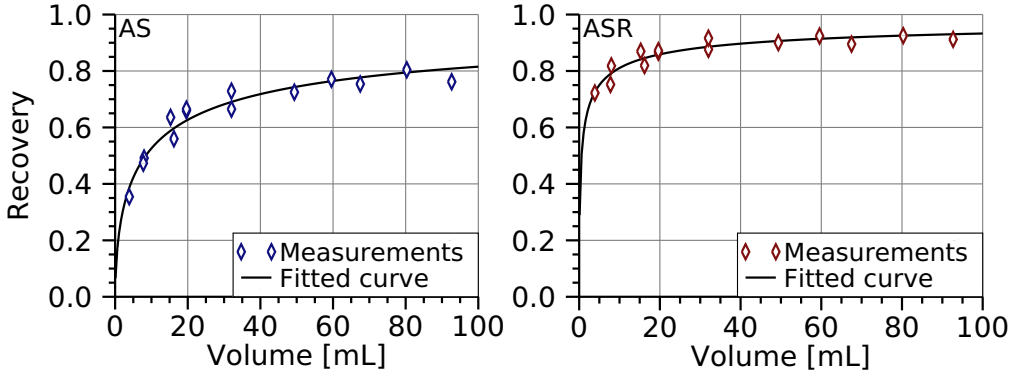
Figure 3.1: Examples of measured recovery values and fitted curves for spherical sources in SPECT images with different reconstruction settings. Left: Results when attenuation and scatter (AS) is modelled in the reconstruction. Right: Results when attenuation, scatter and resolution (ASR) is modelled.

1.1.4 Multiple photopeak method

As mentioned in section 1.1.1 there are a number of methods that can quantify activities, with attenuation factored in, using a single planar gamma camera measurement without source depths measured from a different imaging modality. One class of such methods utilises measurements on multiple photopeaks for estimation of a depth used for attenuation correction and activity quantification. The general idea is that emitted photons with different energies will be attenuated by different amounts, meaning that the relative amounts of counts measured within two or more photopeak windows will depend on the source depth (Strand and Persson, 1977). By comparing the counts measured against reference sensitivities for the camera system, the source depth can be inferred. This type of method is only applicable for sources that features two or more prominent photopeaks, which preferably have a large separation in energy to make the difference in attenuation more marked. Strand and Persson (1977) demonstrates such a method for ^{123}I, using photon emissions at 159 keV and 28 keV. It is also possible to employ multiple radioisotopes to obtain suitable photopeaks for this method, but all radiopharmaceuticals administered must have comparable properties with similar uptake rates and distributions. ^{177}Lu makes an interesting radionuclide for this class of methods, with its three prominent peaks at 55 keV, 113 keV and 208 keV. At present, gamma cameras are often combined with a CT-unit, allowing attenuation maps to be acquired and spatially matched to the emission images rather easily. CT-derived attenuation corrections are typically highly robust and accurate and the multiple-photopeak method is, thus, less relevant now. However, the method may still find use cases for small and hand-held systems, as these cameras typically only perform emission imaging and lack other ways to estimate the source depth. Against this background, Paper v investigated the feasibility of using a multiple-photopeak method to quantify activity with

^{177}Lu and a hand-held CZT-based camera system. The method developed in the paper is described here to illustrate one approach to the depth estimation problem and highlight its drawbacks.
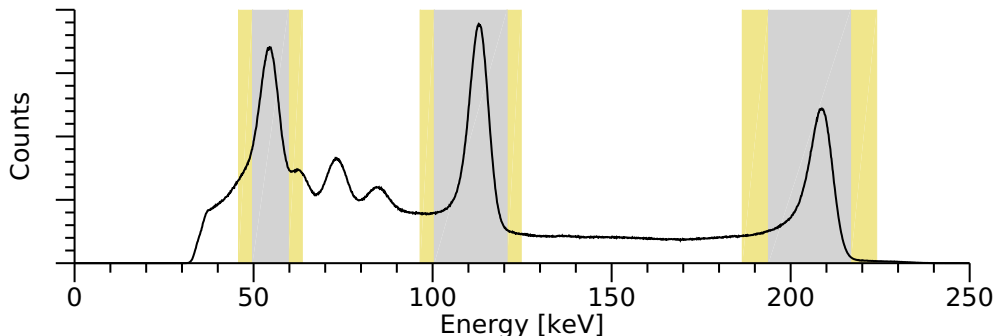
Figure 3.2: Illustration of a ^{177}Lu spectrum and energy windows used for a multiple photopeak method. Main energy windows are shown in grey behind each of the three prominent photopeaks, and TEW scatter windows are shown in yellow.

The basis for any multiple-photopeak method is the measurement of count rates ($R_{i,\mathrm{meas}}$) within two or more photopeak windows (denoted by i). Figure 3.2 illustrates a ^{177}Lu spectrum energy with windows that could be used. The other component of the method is a model of the count rates that can be obtained by the system. This model must depend on the source activity and depth and may further model other aspects, such as the measurement geometry and source size. The general framework is

$$R_{i,\mathrm{model}} = A \cdot \varepsilon_i \cdot D_i, \tag{3.1}$$

where A is the source activity, ε_i is the camera sensitivity and D_i describes the photon attenuation (Strand and Persson, 1977). In Paper v, the model used was

$$R_{i,\mathrm{model}}\left(A,d\right) = A \cdot \varepsilon_i(d) \cdot e^{-\mu_i \cdot d} \cdot B_i\left(d \cdot \mu_i\right), \tag{3.2}$$

where d is the source depth, μ_i is the attenuation coefficient of the attenuating material and B_i is an error factor analogous to the build-up method. Ideally, ε_i would be constant for the parallel-hole collimators used in the paper, but measurements with hand-held cameras are typically made with the camera positioned as close as possible to the source, introducing a depth-dependence due to septal penetration. The sensitivity function can be obtained by fitting an expression to the camera sensitivities measured for a source in air at various distances. For the sensitivity of a parallel-hole collimator with septal penetration, the expression $\varepsilon_i(d) = c_{0,i} + c_{1,i} \cdot e^{-c_{2,i} \cdot d}$ can be used (NEMA, 2013). The term B_i directly corresponds to a build-up factor if no scatter-correction is performed. Due to the energy tailing in CZT camera spectra, conventional scatter correction methods (e.g. TEW) may not be perfectly applicable for such systems (Kacperski et al., 2011), and retaining the term

B_i can, thus, be motivated to correct for smaller errors in scatter-estimation. Paper v uses a simple linear expression based on observations, which is given by $B_i\,(d \cdot \mu_i) = 1 + k_i \cdot d \cdot \mu_i$.

With the measured count rates acquired and a model established, requiring that $R_{i,\mathrm{meas}} = R_{i,\mathrm{model}}$ produces a system of equations to solve. With three main energy windows and equation 3.2, the equation system is overdetermined with three equations and two unknowns (A and d). This problem can be solved a range of methods. In Paper v, the values for A and d were estimated by a weighted least-squares fit between $R_{i,\mathrm{model}}$ and $R_{i,\mathrm{meas}}$ using a gradient-expansion algorithm.

As the modelled count rate for every energy window is equally affected by the source activity, what is most important for the method is the ratio of the count rates between the energy windows. Given a set of measured count rates, the method effectively attempts to find a depth which produces the same ratios as in the model; The activity merely follows as a scale factor that minimises the least-square difference in absolute count rate levels. It is important to ensure that the estimated depths are accurate, as any errors in estimated depth will directly affect the estimated activity. The main driver for such errors is likely inaccuracies in the count rate ratios of the model, which would drive the equation system solver towards an incorrect depth when attempting to match measured and modelled ratios. To minimise depth errors, the count rate ratios should ideally change as much as possible with depth. As a result, the method benefits if there are large differences in attenuation coefficients between the energy windows. However, to minimise systematic errors the model should ideally reproduce the camera measurement as closely as possible, as aspects such as system sensitivity, attenuation, scatter, penetration in conjunction with the source size and source delineation can affect the count rate ratios. Considering these parameters, equation 3.2 represents a simplified model suitable for an initial feasibility study and could be augmented or replaced with a more detailed model in the future.

1.2   Image segmentation

In an image-based activity quantification method, it is necessary to identify any objects of interest and classify or delineate the regions that the objects occupy in order to perform an analysis or measurement of the activity uptake. This process of making delineations and classifications in an image is called image segmentation.

One common segmentation method is manual delineation, in which a human operator identifies and delineates objects in images. This process can, however, be relatively slow and entail a large operator workload. The results may also have inter- and intra-operator variabilities (Breen et al., 2007; Vorwerk et al., 2009). It can, therefore, be advantageous to employ algorithms to handle the delineation. Such methods can typically be considered to be either semi-automatic, where an operator may handle the object identification and have

some input on the segmentation method, or fully automatic, where objects are identified and delineated with minimal operator input.

A common approach in both automatic and semi-automatic segmentation is thresholding, in which a region is classified as belonging to an object based on whether one or more properties of the region satisfy one or more thresholds or intervals of acceptable values. An example of a thresholding operation can be to classify all voxels that have an activity concentration greater than 42 % of a maximum concentration within a rough delineation in a SPECT image as belonging to an object of interest. This segmentation approach is faster and less operator dependent than manual segmentation, but the result can be affected by poor contrast and noise in the image (Rogowska, 2000; Gustafsson et al., 2017).

Another semi-automatic approach to image segmentation is through the use of active contours (Kass et al., 1988). In this approach, an initial contour is created and assigned an internal and external energy. The internal energy is related to the curvature of the contour and exists to keep the contour smooth and free of noisy irregularities. The external energy is based on where the contour is located over the image and exists to attract the contour towards a feature of interest, such as sharp gradients or high or low intensities within the image. Image segmentation is performed using an iterative approach, in which the contour is successively moved in such a way that the sum of the internal and external energy is gradually minimised. Active contour methods are also referred to as 'snakes', as contours (in two-dimensional images) tend to show slithering motions as they adjust to minimise their energy. Different features can be delineated depending on how the external energy is defined. Defining an external energy that it is low where there are sharp gradients in the image will, for instance, create a contour that will move towards edges in the image. An external energy that is proportional to the image intensity will result in a contour that attempts to follow valleys or ridges in the image. In gamma camera images, objects of interest can typically be identified by a sharp change in activity uptake compared to their surroundings, making delineations based on image gradients favourable.

2 Internal dosimetry

A commonly used quantity for describing the amount energy that has been deposited from ionising radiation into a medium is the absorbed dose (AD). The AD (D) is defined as the amount of energy absorbed from ionising radiation $\mathrm{d}\bar{\varepsilon}$ by a mass $\mathrm{d}m$,

$$D = \frac{\mathrm{d}\bar{\varepsilon}}{\mathrm{d}m}. \tag{3.3}$$

The unit for AD is Gy, which equals J kg^{-1}. In nuclear medicine, ionising radiation emitted as part of the decay of an administered radioisotope constitutes a source of absorbed doses.

Following the decay of a radioisotope, a number of particles will be emitted (electrons, gammas, x-rays etc.) as the nucleus and its electron shell transitions to lower energy levels (Krane and Halliday, 1987). Each emitted particle will propagate from the point-of-decay and can either escape the patient without any interactions or may deposit all or part of its energy along its propagation path. Energy depositions in patients as a result of individual decays generally cannot be measured, and, instead, an expectation-value for the absorbed dose rate can be calculated from the total activity and the distribution of the radiopharmaceutical.

Typically, the ADs and AD-rates in internal dosimetry are calculated following the medical internal radiation dose (MIRD) formalism (Loevinger and Berman, 1968; Bolch et al., 2009). To facilitate a practically achievable method for dosimetry, this framework employs a number of simplifications. Most notable, the framework concerns average AD-rates to a finite number of regions with non-zero volumes, rather than infinitesimally small points as in equation 3.3. Furthermore, activity is assumed to be uniformly distributed within each of the regions concerned. With these assumptions, the AD-rate to a region at a time t after administration of a radiopharmaceutical is calculated as

$$\dot{D}\left(r_T, t\right) = \sum_{r_S} A\left(r_S, t\right) \cdot S\left(r_T \leftarrow r_S, t\right). \tag{3.4}$$

Here, r_T denotes a target region for which the AD-rate $\dot{D}\left(r_T, t\right)$ is calculated, and r_S denotes a source region containing a uniformly distributed activity $A\left(r_S, t\right)$. The quantity $S\left(r_T \leftarrow r_S, t\right)$ represents the average AD that the region r_S receives per decay that occurs in the region r_S. The regions r_T and r_S commonly represent whole organs, but can also correspond to smaller regions, such as organ parts, tumours, cells, or cell components. Individual voxels in images can also be represented by the regions (Bolch et al., 2009). The mean AD to r_T is calculated by integrating $\dot{D}\left(r_T, t\right)$ over a time-period T_D of interest:

$$D\left(r_T, T_D\right) = \int_0^{T_D} \dot{D}\left(r_T, t\right) \mathrm{d}t = \int_0^{T_D} \sum_{r_S} A\left(r_S, t\right) \cdot S\left(r_T \leftarrow r_S, t\right) \mathrm{d}t. \tag{3.5}$$

Equations 3.4 and 3.5 represent the more general form of the MIRD formalism, where S can change over time, e.g. as the regions grow, shrink or move. For many circumstances, it is possible to approximate with good accuracy that S does not change markedly during the time that the majority of the AD is delivered. With a time-independent S, equation 3.5 can be written as

$$D\left(r_T, T_D\right) = \sum_{r_S} \tilde{A}\left(r_S, T_D\right) \cdot S\left(r_T \leftarrow r_S\right), \tag{3.6}$$

where $\tilde{A}\left(r_S, T_D\right) = \int_0^{T_D} A\left(r_S, t\right) \mathrm{d}t$ is the cumulative, or time-integrated activity of region r_S. As the unit of $A\left(r_S, t\right)$ is Bq or s^{-1}, $\tilde{A}\left(r_S, T_D\right)$ is unitless and indicates the

total number of decays that have occurred in region r_S. It is, however, typical to express cumulated activities in equivalent units of MBq h.

As best presented by equation 3.6, the MIRD formalism divides the task of dosimetry calculations into two steps: determination of the activity uptake in a number of regions, either over time or as the total cumulated activity, and the calculation of quantities that relates the activity uptakes to ADs or AD-rates. I.e. one task deals with activity quantification and tracking the radiopharmaceutical distribution over time, while the other task deals with calculations of radiation transport and radiation interactions with matter.

2.1 S-values

The quantity $S\left(r_T \leftarrow r_S, t\right)$ is typically called an S-value. This quantity relates to how energy that is emitted for a decay in region r_S is absorbed in region r_T. The S-values depend in part on the characteristic emissions of the radionuclide in question, factoring in the possible particle types, particle energies and emission probabilities, and depend in part on factors affecting the transport of radiation from r_S to r_T, such as the distance between r_S and r_T and the tissue compositions of all regions nearby and in-between. The quantity $S\left(r_T \leftarrow r_S, t\right)$ is given by the equation

$$S\left(r_T \leftarrow r_S, t\right) = \frac{1}{M\left(r_T, t\right)} \sum_i E_i \cdot Y_i \cdot \phi\left(r_T \leftarrow r_S, E_i, t\right), \qquad (3.7)$$

where $M\left(r_T, t\right)$ is the mass of the target region, i refers to the possible emissions by the radionuclide, which have energies E_i and yields Y_i, and ϕ is the fraction of the energy E_i emitted from r_S that is absorbed in r_T.

Tables of pre-calculated S-values can often be obtained for commonly used radionuclides for organ-level dosimetry. These are typically calculated using anthropomorphic computer phantoms and Monte Carlo simulation programs. The exact values of $S\left(r_T \leftarrow r_S, t\right)$ can vary between patients and tabulated S-values are typically provided for different computer phantoms, representing average adults and children and at a few different age points (Andersson et al., 2017; Chauvin et al., 2020). Many types of computer phantoms have been developed, ranging from simple phantoms with structures defined by geometric shapes to highly realistic phantoms with structures defined via advanced 3D-modelling techniques (Snyder et al., 1969; Segars et al., 2010; Segars et al., 2013). Pre-calculated S-values may be suitable for dosimetric calculations for diagnostic examinations, where absorbed doses are low, but individualised calculations may be warranted for therapeutic applications where accurate AD estimates are required for organs at risk or tumours. Individualised dosimetry can be performed using Monte Carlo programs as well, using, for example, CT-images to support radiation transport calculations. Given a SPECT/CT-image, there are programs

capable of deriving a dose-rate image from the activity distribution in the SPECT-image, effectively calculating S-values for equation 3.4 on-the-fly.

2.2 Time-activity determination

The other aspect of internal dosimetry calculations is the determination of activity-curves $A(r_S, t)$. In many cases, the quantity of primary interest is the final cumulative activity $(\tilde{A}(r_S, T_D))$ in each relevant source region. Having full knowledge of the time-activity curve may be of interest if the S-values are expected to change notably during the treatment, or if biological effects shall be modelled, for which the delivered AD-rates matter.

The are many ways that $A(r_S, t)$ can be estimated. Direct measurement methods include gamma camera imaging, as well as non-imaging techniques, such as tissue biopsy and blood or urine sampling (Bolch et al., 2009). It is also possible to estimate activity curves indirectly through pharmacokinetic models, which simulate the various source regions as a series of compartments and define the uptake and redistribution of a pharmaceutical using differential equations linking various compartments (Bolch et al., 2009; Brolin et al., 2015).

Measurements on their own only produce a finite number of activity estimates. To obtain a complete continuous activity curve, measured data points needs to be combined with some method that infers a full curve. Pharmacokinetic compartment models represent a highly advanced option, for which measured data can be used to fine-tune the parameters of the differential equations. More typically, simpler and more accessible methods are used to obtain complete curves. Examples of common methods includes performing a simple interpolation between the data-points, possibly combined with a mono-exponential function for extrapolation, and curve fitting. Figure 3.3 shows an example of the result from a curve-fitting approach, where the activity in a tumour has been measured at four data points using gamma camera images and a fitted expression has been used to infer the full activity curve.

2.2.1 Gamma camera imaging protocols

Regarding activity curve estimation from gamma camera imaging, there are a number of possible approaches as for how the gamma camera is used. Activity quantification based on SPECT images is more accurate, as the correction methods can be made more precise when working with the full three-dimensional activity distribution and when density information from a CT is available. Planar activity quantification is less accurate, as correction methods that deal with two-dimensional information must be more approximative. Furthermore, the lack of depth-information in planar images means that activity estimates for a given region may be affected by activities in any over- and under-lying regions. Planar
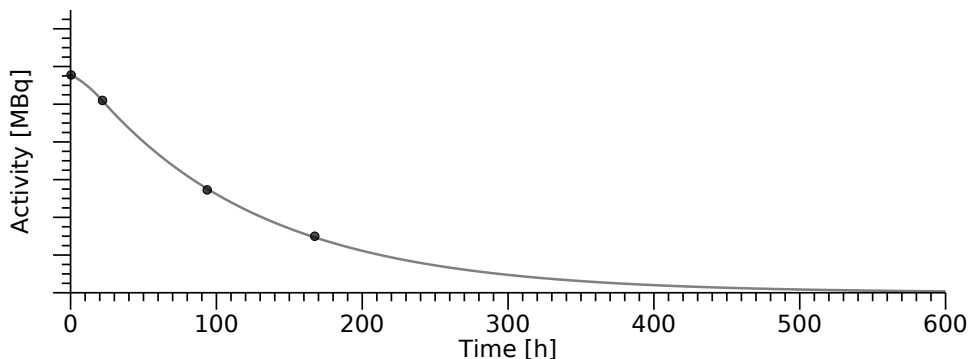
Figure 3.3: Example of a time-activity curve for one tumour during radionuclide therapy with [^{177}Lu]Lu-DOTA-TATE. Measurements are shown with black points and a fitted curve is shown with a solid line. The fitted curve consists of a second-degree polynomial from the start to the second measurement point and a mono-exponential component from the second measurement point and onwards.

imaging does, however, have some advantages: General-purpose gamma cameras typically have a FOV in the order of $50 \times 50 \, cm^2$, meaning that acquisitions must be made with the camera at multiple bed positions if whole-body imaging is of interest. For whole-body imaging, planar acquisitions may be more feasible than SPECT acquisitions, taking into consideration image noise and the maximum measurement times imposed by patient comfort. Planar images may also impose a smaller work-burden on operators regarding delineations compared with SPECT images, especially if a manual or less automated delineation method is used.

The pros and cons of planar and SPECT imaging gives rise to three typical imaging protocols: planar imaging at all time-points, SPECT imaging at all time-points and hybrid methods with planar imaging at multiple time-points and SPECT imaging at one or a few times. Each method has different strengths related to the advantages and disadvantages listed in the previous paragraph. Hybrid planar-SPECT approaches attempt to capture the advantages of both methods, providing the practicalities of planar whole-body imaging with the accurate activity estimates of SPECT imaging. The underlying assumption of a hybrid approach is that the general shape of the time-activity curve can be estimated with sufficient accuracy from the planar images, but the absolute curve amplitude may be inaccurate. Scaling the planar-derived curve to fit the activity estimated from a single SPECT image mitigates this potential inaccuracy. Figure 3.4 illustrates the principle of the hybrid method.

In addition to the planar, SPECT and hybrid approaches, there are a number of simplified methods that aim to estimate the cumulative activity using a reduced number of image acquisitions. The most drastic methods require only a single SPECT image, which provides sufficiently accurate AD estimates if the time at which imaging is performed is selected
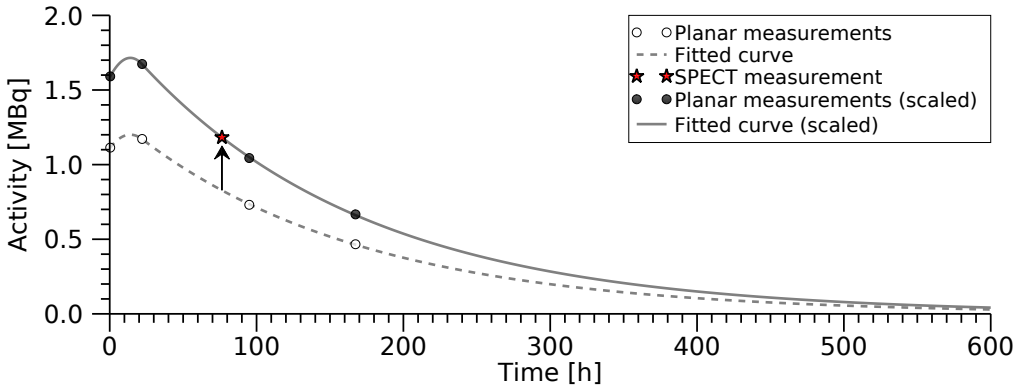
Figure 3.4: Example of a hybrid planar-SPECT time-activity curve for one tumour during radionuclide therapy with [^{177}Lu]Lu-DOTA-TATE. Planar measurements are shown with open circles, and a fitted curve is shown with a dashed line. The activity measured from a SPECT image is shown with a star, to which the planar measurements and curve have been scaled (solid circles and line).

carefully (Hänscheid et al., 2018; Jackson et al., 2020). For therapies where a radiopharmaceutical is administered over multiple cycles, a possible approach is to acquire an activity curve from a full set of images at the first treatment cycle and assume that this curve is applicable in subsequent cycles. Alternatively, a single SPECT image can be acquired at each subsequent cycle to scale the original activity curve (Sundlöv et al., 2018). These approaches operate under various assumptions for the time-activity curve, such as a similarity in curve shape between patients or across treatment cycles. Before implementing any simplified methods, information about typical time-activity curves and their behaviours across cycles should be obtained to guide the choice of method and ensure that estimated ADs will be sufficiently accurate.

3   Tumour studies alongside the Iluminet trial

The Iluminet trial (EudraCT number 2011-000240-16) is a phase 2 study evaluating the safety and efficacy of a dosimetry-driven treatment of patients with NETs using [^{177}Lu]Lu-DOTA-TATE conducted at two Swedish hospitals. Approximately 100 patients are included in the study. Treatment is given in a variable number of cycles with 7.4 GBq [^{177}Lu]Lu-DOTA-TATE administered at each cycle. The number of cycles administered to a patient is decided based on the biologically effective dose to the kidneys, with a target in cumulative dose of 27 Gy or 40 Gy depending on assessed risk factors for each patient (Sundlöv et al., 2017). Gamma camera images are acquired in every treatment cycle as a basis for the dosimetric calculations. The imaging protocol consists of planar whole-body conjugate-view imaging at four time-points, roughly 1 h, 24 h, 96 h and 168 h after [^{177}Lu]Lu-DOTA-TATE infusion. At the 24 h time-point, a planar CT-localiser is also

acquired, along with a SPECT/CT covering the length of a single FOV positioned over the thorax and kidneys.

The planar images are processed to produce two-dimensional activity maps using a pixel-based method. This method consists of co-registering all planar images to the CT-localiser, performing attenuation-correction using a conjugate-view method with an attenuation map derived from the CT-localiser and performing scatter correction through a scatter-kernel deconvolution (Sjögreen Gleisner, 2012; Sjögreen Gleisner and Ljungberg, 2012). The SPECT is reconstructed with an ML-EM-based reconstruction program to produce quantitative images. The SPECT-images are further used as inputs to a Monte Carlo program to produce dose-rate images. The kidney dosimetry procedure involves using the planar images to produce kidney time-activity curves, which are then scaled to fit associated dose-rates estimated from the dose-rate images (Sundlöv et al., 2017; Sundlöv et al., 2018).

3.1   A tumour dosimetry workflow

A large portion of the projects in this thesis have been performed with patients and images from the Iluminet study and the focus has been on tumours. Tumour dosimetry presents different challenges compared with kidney dosimetry, as NET metastases may be quite numerous and present a highly heterogeneous assembly in terms of sizes and surrounding structures. Hence, two papers (Paper I and Paper IV) are dedicated to evaluations of tumour dosimetry aspects within the images acquired in the study.

As many NETs can be comparably small, there is a concern that estimated cumulative activities and ADs to tumours may be inaccurate. The available SPECT images have been found to be accurate for activity quantification with tumour volumes down to approximately 8 mL (Gustafsson et al., 2017), but the use of planar images to estimate activity curve shapes can impose additional limitations on suitable tumours: as planar images present the sum of activities within multiple over- and under-lying regions, the estimated activity curves will always represent some combination of the curves from multiple regions and there are, thus, concerns that a hybrid planar-SPECT approach may be unsuitable for some tumours. Additionally, the large number of images acquired per patient over all cycles means that the operator workload and segmentation repeatability may need to be addressed, especially if many tumours are to be evaluated per patient.

Against this background, Paper I set out to establish a workflow for tumour dosimetry suitable for the Iluminet images and investigate the accuracy of tumour ADs. Central to the presented workflow is a program developed, which loads and displays all images (planar, CT-localiser, SPECT/CT) belonging to a selected treatment cycle. The program also holds the delineations made for all identified tumours in both the planar and SPECT images and, thus, is effectively a centralised program for tracking all information needed for tu-

mour dosimetry. The planar images are co-registered to SPECT/CT images, making the task of identifying the same tumour in both images much easier. Planar image segmentation is carried out semi-automatically within the program using a method based on active rays (Denzler and Niemann, 1999), in which a polar transformation is applied to the planar images and segmentation is carried out using an active contour approach (Kass et al., 1988). SPECT segmentation is performed semi-automatically by interfacing to a separate dedicated program, which provides a Fourier-surface based segmentation method (Gustafsson et al., 2017). Planar activity curves are obtained through curve fittings, which are performed by interfacing with routines from the LundaDose program. Overall, the program makes tumour dosimetry practical and Paper I shows that sufficiently accurate dosimetry can be performed for many tumours, but those that have a noticeable proportion of overlapping activity from over- or under-lying regions should be excluded.
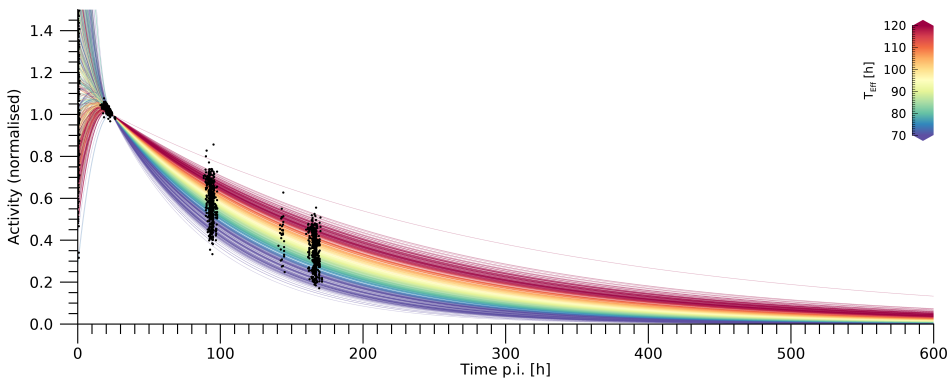
Figure 3.5: Illustration of time-activity curves for tumours during radionuclide therapy with [^{177}Lu]Lu-DOTA-TATE. Measurements are shown using black points and fitted curves are shown by coloured lines. The curves have been normalised to have the value 1.0 at 24 h, and are colour-coded based on their effective half-lives (T_{eff}).

In Paper I, the program is applied and evaluated in a smaller set of patients and cycles, limited to certain cycles where planar and SPECT images were acquired at all time-points. Leading up to Paper IV, the tumour dosimetry program is applied to nearly all Iluminet images acquired in Lund. The results acquired allow for tumours ADs and dosimetric parameters to be evaluated across treatment cycles, which Paper IV focuses on. The results acquired may also be used to study AD-effect relationships for NETs, but this has been left for a separate future project. Paper IV shows that tumours present activity curves with a wide range of effective half-lives, but that the half-life of a given tumour is typically show limited variation between treatment cycles. Figure 3.5 illustrates nearly all of the time-activity curves acquired. Any changes in tumour ADs between cycles can in large part be attributed to changes in overall activity uptake amplitude. This means that simplified dosimetry methods that assume that all tumours have the same shape for the time-activity curve may be less accurate, but the class of approaches that features image acquisitions at multiple time-points at the first cycle and a single SPECT acquisition at subsequent cycles

may be adequate.

3.2 Hand-held gamma camera applications

In addition to the tumour dosimetry projects in Paper I and Paper IV, imaging of superficial tumours has also been carried out with a hand-held gamma camera (Figure 2.12) for two patients in the Iluminet trial. The hand-held camera is interesting and promising, as it offers the opportunity to image tumours with better resolution and could provide additional sample points for activity-curve investigations. The main drawback of the camera can be considered to be its small FOV, which limits the structures that can be feasibly imaged. Additionally, the camera is CZT-based and behaves differently compared to conventional Anger cameras. The novel behaviour has warranted detailed studies of the camera through characterisation measurements (Paper II) and computer simulations (Paper III). Paper II and Paper III can be considered to represent two steps on the route to performing activity quantification with the camera, which Paper V concludes. The camera is easy to work with and has proven to be a valuable research tool, providing an increased understanding into CZT cameras. The camera incorporates a single CZT module, which is a self-contained package containing the CZT crystal and all of the readout-electronics necessary. Larger CZT-based gamma cameras are typically made by arranging such modules in tiles. As the specification for the module in the hand-held camera is similar to those of larger cameras, the general findings made with hand-held camera may be applicable to those cameras as well.

Chapter 4

Gamma camera modelling and simulation

Computer models of imaging systems are useful tools for improving the understanding of the image formation process (Jan et al., 2004). Computer models offers several advantages, such as the possibility to study features that are difficult to isolate or measure with physical measurements. A principal example is the isolation of the contributions to an acquired image from different categories of photons, such as primary, scattered and penetrating photons. Computer models can also be preferable if large sets of measurements are to be acquired, as simulations can easily be queued up with some parameter of interest precisely controlled and adjusted (e.g. acquisition time or source-collimator distance).

1   Common aspects

To model a measurement with a gamma camera, there are a number of steps that need to be considered (Prettyman, 1999). These steps include:

- Emission of radiation within a source

- Propagation of radiation through intermediary matter towards the camera

- Radiation interaction in the detector crystal

- Transport of information carriers within the detector crystal

- Generation of electrical output signals from the detector sensors (e.g. outputs currents from anode contact pads or PM tubes)

- Processing of these output signals in pre-amplifiers etc.

- Further decisions for image or spectrum formation

Accurate modelling of the radiation transport is necessary for essentially every detector model. The transport of radiation is associated with a number of possible interaction processes with matter, which are all stochastic with likelihoods and outcomes described by cross-sections and probability distributions. The exact paths of individual particles cannot be predicted in advance, and the camera system output can consequently also not be predicted precisely for a given measurement. What can be estimated from a model involving radiation transport is an expectation value of the system output. The Monte Carlo method is a powerful technique that has the potential to accurately estimate expectation values for this kind of problem. The general principle is to instantiate and propagate a single particle at a time, while considering all possible interactions that can affect it (Ljungberg and Strand, 1989; Rogers and Bielajew, 1990). Given the position and propagation direction of a particle, one can determine the probability distribution for how long the particle will travel until an interaction occurs with the surrounding matter. The propagation of a particle is realised by drawing a random range from this distribution and moving the particle by this distance. A random number generator is used for this purpose, typically in the form of a pseudo-random number algorithm. Which interaction process the particle undergoes and the outcome (absorption or change in energy and direction) is further decided by considering the processes and probabilities involved and using random numbers. The particle transport procedure is repeated until the particle is absorbed or escapes the simulated world. Useful outputs from the simulation are obtained by processing all particle interactions within the detector crystal in dedicated routines, responsible for modelling the signal generation processes, readout-electronics and assemble resulting images or spectra. By finding the average outcome from many particle histories, the Monte Carlo method is able to estimate the expectation value of different quantities. The Monte Carlo method is computationally expensive, but can be more accurate than approximative analytical solutions.

The steps associated with the camera system may have varying degrees of importance depending on the modelled detector. For instance, the energy spectrum of a scintillation detector can in large part be governed by the radiation transport, fluctuations in the number of created scintillation photons, and electronic noise, but the transport of scintillation light (information carriers) within the camera crystal may have a lesser importance and could be included as a fixed collection efficiency rather than be modelled in detail. For compound semiconductor detectors, phenomena during the charge carrier transport can have a much larger impact on the detector behaviour and may therefore require more detailed modelling.

2   Considerations for pixelated CZT cameras

For CZT-based cameras the detector response strongly depends on the position within the crystal volume where an interaction occurs. This response is determined by the charge carrier transport and signal induction processes, which are described in detail in Chapter 2. Modelling these processes allows for the characterisation of individual electrodes in the form of CIE maps, which store the electrode responses for all possible interaction positions throughout the detector volume. For an anode element in a pixelated detector, the CIE map can typically be described as having a plateau with the highest induced signals for interaction positions underneath the anode contact pad, at depths near the cathode. For interaction positions close to the anode-side, the induced signal tends to decrease due to the poor transport of holes. Within the region underneath the surrounding gaps the induced signal gradually decreases as the neighbouring anodes receives an increasing portion of the induced signal. As demonstrated in Chapter 2, the readout-electronics attached to an anode will tend to underestimate the energies of incident photons that interact at positions where the CIE map values are lower than on its plateau, leading to low-energy tails in the energy spectrum. The exact magnitude of the low-energy tails is governed by the shape of the CIE map and the spatial distribution of photon interactions in the detector crystal. Depth-wise, the number of photon interactions will decrease following an attenuation curve determined by the photon energy. Lower-energy photons will tend to interact primarily at shallow depths with similar CIE-values, reducing the magnitude of the low-energy tails compared to those of more energetic photons with more uniform interaction-distributions across the depth. The distribution of photon interactions can also vary laterally throughout the detector volume if a collimator is used, as the collimator walls will shield parts of the crystal. Collimators with holes aligned to the anode elements (matched collimators) in particular require special considerations, as this design produces a systematic shielding of the inter-anode gaps (Figure 4.1). Such collimators may consequently reduce the low-energy tails as the likelihood of interactions over the lateral edges of the anode CIE maps decreases. Matched collimators should thus not be simulated through any simplified analytical methods, but rather using ray-tracing or equivalent methods that accounts for the position and geometry of the collimator walls (Ljungberg et al., 2005). To obtain a CZT detector model that accurately reproduces the response of an existing system, the factors described make it evident that finding the correct shape of the CIE maps is a fundamental requirement. Roughly speaking, the task of finding the correct CIE map can be divided into the tasks of finding the correct depth-dependence and finding the correct lateral shape.
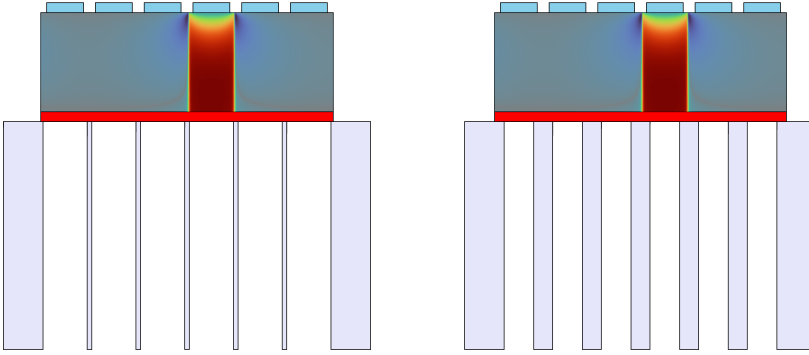
Figure 4.1: Cross-sections of two camera system with matched collimators. The semiconductor crystal is shown in grey, the cathode in red and the anode contact pads in blue. Parallel-hole collimators are shown in light grey. The wall-thicknesses of the left and right systems correspond to low- and medium-energy collimators, respectively. A CIE map is shown for one anode element within each system.

2.1 Numerical calculations

To build a semiconductor detector model, it is necessary to implement the charge transport and signal generation equations in some manner. The equations can be analytically solved for simpler geometries, e.g. in a parallel-plate detector with uniform electric field and no diffusion (Hecht, 1932; Guerra et al., 2008; Knoll, 2010). The weighting potential can be analytically calculated for more complex electrode configurations, but this involves infinite sums (Castoldi et al., 1996). To obtain more feasible analytical expressions, approximations of the weighting potential shape or the motions of charges are typically used (Hamel and Paquet, 1996; Guerra et al., 2008; Pretorius et al., 2015). For instance, the weighting potential could be assumed to be a function of depth only, or charge motion could be considered in one dimension only. Using such approximations may affect the accuracy of the model, for instance if the shape of the CIE map is markedly affected or if an important aspect of the detector response is omitted. As an example, it is possible for negative signals to be generated for certain interaction positions in pixelated detectors (Eskin et al., 1999), which can be difficult or impossible to reproduce with a one-dimensional weighting potential, as this is linked to the weighting potential 'extending' into the region below a neighbouring anode pad. To fully consider the transport and signal generation equations in three dimensions, the alternative approach is typically to solve the equations numerically. A number of different numerical approaches are possible, common methods being the finite difference method (Press et al., 2007; Jung et al., 2006) and the finite element method (d'Aillon et al., 2006; Myronakis and Darambara, 2011). The finite difference method is comparably easy to implement, and in Paper III this approach is used. Details regarding the method are provided in Appendix B.

To summarise Appendix B, the finite difference method introduces a grid of points within

the detector volume. The spatial derivatives in a given differential equation are approximated by differences in values between neighbouring grid points. For differential equations involving only spatial derivatives (e.g. equation 2.5), the finite difference method produces a system of linear equations with one equation per grid-point. Solving the equation system yields an numerical solution to the differential equation, i.e. values of the unknown function on the grid. For differential equations involving spatial and temporal derivatives, the unknown function is iterated forward in time from a known initial state, producing either values of the unknown function on a spatial and temporal grid or the final state on a spatial grid.

For models involving numerical methods, determining a CIE map is a useful end-goal, as this map will describe the detector response for all interaction points on a grid. A pre-calculated CIE map makes it possible to avoid simultaneous evaluation of the charge transport equations and modelling of the photon interactions. This is in contrast to analytical approaches with less computationally expensive approximations, which can compute aspects of the charge transport continuously and thus do not require explicit CIE maps (Guerra et al., 2008; Pretorius et al., 2015).

To numerically calculate a CIE map, the best approach is to solve the adjoint transport equations (Appendix A, equations A.1 and A.2). These in turn depend on an electric potential and weighting potential (equations 2.5 and 2.7). Hence, the numerical calculation of a CIE map can be condensed into three main steps:

1. Calculate the electric potential of the detector (solve equation 2.5)

2. Pick one electrode and calculate its weighting potential (solve equation 2.7)

3. Calculate the CIE map for one of the charge carriers by solving its adjoint transport equation (equation A.1 or A.2)

2.2 A full detector implementation

A CIE map describes the induced charge on a single anode following a radiation interaction. It is an important quantity that encompasses the mechanisms involved in the charge transport and signal generation, but does not characterise the full detector. To form a complete detector model, CIE maps needs to be considered alongside the final step in the radiation detector system: the pulse-processing in the readout-electronics and the subsequent image or energy-spectrum formation. This includes factors such as noise from fluctuations in the number of created electron-hole pairs and electronic noise, and how the readout-electronics attached to the anode processes the induced current. Furthermore, a pixelated detector will contain many anodes with individual readout-electronics, and an incident photon may generate signals in more than one anode, which Figure 4.2 demonstrates. A full model needs

to reproduce how the detector circuitry and microcontrollers deal with cases of multiple anode signals. Simpler systems may for instance be designed to only retain the first or largest signal, whereas more advanced systems could retain the signals of a neighbourhood to estimate the interaction position at a sub-pixel level (Peterson and Furenlid, 2011; Kim et al., 2013). A summary of a complete camera model is shown in Figure 4.3, demonstrating the geometrical and electronic arrangements that need to be considered.
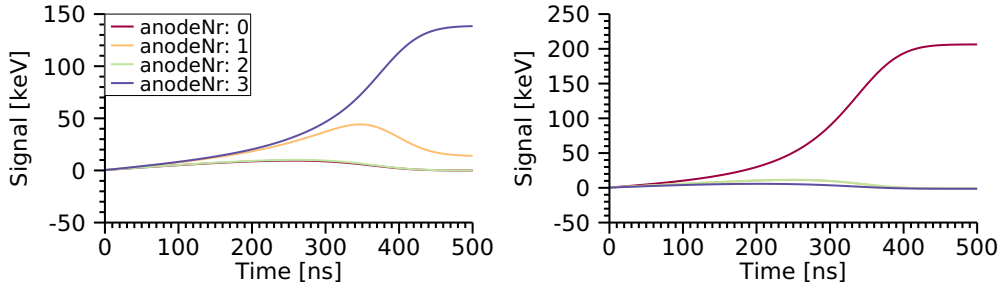

Figure 4.2: Example of signal pulses produced by four anodes (2 × 2 arrangement) in a time-dependent detector model. The left and right graph each relates to an incident 208 keV photon. The pulses correspond to induced charges (equation 2.12), rescaled to energy in keV for convenience.

In Paper III, a full detector model was designed and implemented. The aim was reproduce the behaviour of the hand-held camera mentioned earlier (Chapter 2, Section 4.1), and important components of the detector model, based on what was known about the camera, included:

- A single solid state CZT detector module is integrated into the camera (OMS40-G256, Orbotech Medical Solutions Ltd., Israel). This module has been characterised by Kotoch et al. (2011). Vadawale et al. (2009) presents further characterisations of a similar but unspecified module.

- The CZT crystal size is $39 \times 39 \times 5 \, \text{mm}^3$. One side is fully covered by a cathode and the opposing side is covered by an array of 16×16 anodes, each with a $1.86 \times 1.86 \, \text{mm}^2$ contact pad. The pitch between neighbouring anodes is 2.46 mm, leaving a 0.6 mm gap between each anode.

- The hand-held camera operates with a 600 V potential is applied over the crystal.

- It is believed that only one anode element signal is kept for each incident photon, likely the one whose signal first exceeds a set threshold.

Parameters that were unknown or less certain were

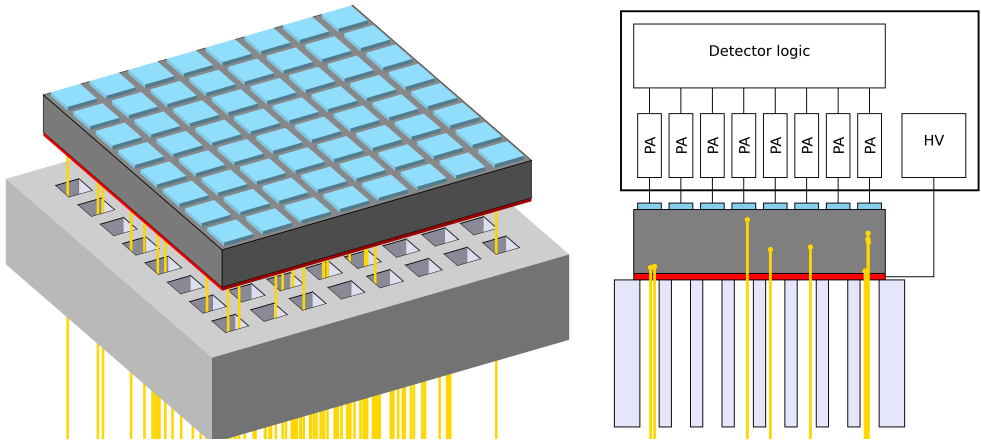- The exact values for the electron and hole mobilities and lifetimes

Figure 4.3: Illustration of a pixelated semiconductor detector coupled with a collimator and readout-electronics. The semiconductor crystal is shown in grey, the cathode in red and the anode contact pads in blue. A parallel-hole collimator is shown underneath the crystal in light grey. Photon tracks are shown in yellow. PA: pulse analyser. HV: high voltage.

- Time-constants of the readout-electronics, such as the signal integration times and time-constants affecting the processed pulse shapes.

- Electronic noise characteristics and its influence on the cameras energy resolution.

- The exact shapes of the electric and weighting potentials, or more specifically how they behaved in the inter-anode gaps.

Ideally, each anode has its own unique CIE map describing all time-dependent output pulses it can produce. However, determining a unique CIE for each anode is computationally expensive, as in the case of the hand-held camera, there are 256 anodes. Furthermore, knowing the full signal pulses is less relevant if the parameters of the readout-electronics are not known. Given these two issues, a practical solution is to assign all anodes a joint CIE map, corresponding to a long or infinite integration time:

$$\eta_{\text{joint}}\left(\vec{r}\right) \sim \lim_{t \to \infty} \eta_{\text{joint}}\left(\vec{r}, t\right), \tag{4.1}$$

$$\eta_k\left(\vec{r}\right) = \eta_{\text{joint}}\left(\vec{r} + \vec{r}_k - \vec{r}_{\text{joint}}\right). \tag{4.2}$$

In these equations $\eta_{\text{joint}}\left(\vec{r}\right)$ is the only CIE map determined through the charge transport and signal generation equations, and is calculated for an anode centred over $\vec{r}_{\text{joint}}$. Correspondingly, $\eta_k\left(\vec{r}\right)$ is the CIE map of anode k, obtained by applying a suitable translation to the joint map.

If fully modelled, the energy deposited by an incident photon would create charge clouds with total charges determined by the average energy required to form an electron-hole pair. The motion of the clouds would induce a charge on an electrode determined by the

initial cloud charge and the charge induction efficiency. Through the readout-electronics this induced charge would be converted into a sequence of signal voltages, which would ultimately be converted into a channel number by an MCA. Governed by the camera system's energy calibration, this channel number would then be converted into an energy measured in keV. If these steps are not known, the simplest solution is to assume that a set of photon interactions in the detector would result in an output signal

$$E_{\text{out},k} = \sum_{i \in H} E_i \cdot \eta_k \left(\vec{r}_i \right), \tag{4.3}$$

where i denotes a single photon interaction wherein an energy E_i is deposited at a position r_i, and H is the set of all interactions belonging to a given photon history. Given that a numerical method has been used to calculate the CIE maps, η_k is available as an array, and $\eta_k \left(\vec{r}_i \right)$ needs to be evaluated through an interpolation. The signal $E_{\text{out},k}$ is proportional to what the output, measured in channel numbers, would have been from a more detailed model. Although the signal is now measured in keV directly, it will be lower than the total deposited energy as $\eta_k < 1$ and needs to be adjusted though an energy calibration, analogous to the calibration step in the more detailed model.

For a detailed detector model, all sources affecting the energy resolution of the detector would each be characterised. Important factors includes fluctuations in the number of electron-hole pairs created, in the number of trapped charges and electronic noise related to leakage-currents (Bolotnikov et al., 2005). To properly reproduce the energy resolution of the modelled detector, a random fluctuation should be added to $E_{\text{out},k}$ based on the noise model. For gamma camera end-users, characterising these noise sources directly may not be possible, and the alternative approach is to infer the noise characteristics from measured energy spectra. It should then be noted that the low-energy tails themselves introduce some widening of the photopeaks. For application of the measured energy resolution to $E_{\text{out},k}$, it must first be altered such that the combined effects of the energy-tailing and the noise model match the measurements.

Equation 4.3 should be evaluated to find the signal pulses for each anode. In the case of the hand-held camera, only the signal from one anode should be kept for each photon history. Ideally the anode would be selected based on signal timings, but this is not possible without a time-dependent CIE map and parameters for the readout-electronics. As a substitute the anode with the largest value for $E_{\text{out},k}$ can be selected, under the reasoning that the anode with largest final signal is more likely to exceed the threshold first.

2.2.1 Approximative solutions

For camera system end-users, the possibility of directly measuring properties of the semi-conductor crystal and readout-electronics may be limited. The alternative is then to con-

struct a model that include approximations whose parameter values are indirectly inferred by tuning the model results towards measured data. Examples of assumptions and approximations include:

- Treating the electron and hole cloud properties, mainly the mobilities and lifetimes, as free parameters. The crystal temperature may also be uncertain, inviting the diffusion constants to be treated as adjustable parameters as well.

- For the shape of the electric potential:

    – Assume that the electric field is uniform, i.e. the electric potential increases linearly from the cathode-side to the anode-side (Hamel and Paquet, 1996; Mardor et al., 2001; Guerra et al., 2008; Pretorius et al., 2015). This introduces no additional parameters to the model.

    – Assume that gradient of the electric field across crystal surface in the inter-anode gaps is zero (when solving equation 2.5). This corresponds to an ideal non-conductive crystal surface, and causes the electric field lines to bend towards the anode contact pads with no field lines ending in the gaps (Richter et al., 1996; Bolotnikov et al., 1999). This assumption introduces no additional parameters to the model.

    – For imperfect materials, the electric potential can be something in-between these two alternatives, with some fraction of the field lines terminating in the gaps (Richter et al., 1996; Bolotnikov et al., 1999; Prettyman et al., 2001). An electric potential resembling this situation can be obtained as a linear combination of the results from the two former alternatives, which introduces one unknown parameter to the model.

- By definition, the weighting potential has a value of unity on one electrode and zero on all other electrodes. The unknown aspect is again related to the shape near the inter-anode gaps, i.e. how the transition from unity to zero across the gaps is made. Methods for obtaining a weighting potential includes:

    – Impose a condition on the gradient across crystal surface in the inter-anode gaps (Tousignant et al., 2000; Mardor et al., 2001; Mathy et al., 2004; d'Aillon et al., 2005). In some circumstances, the gradient across the gaps can be assumed to be zero (Mardor et al., 2001). This introduces no additional parameters to the model.

    – Assume that the weighting potential decreases linearly from unity to zero across the gap between neighbouring anode contact pads (Mayer et al., 1997). This introduces no additional parameters to the model.

- Building on the linear approximation, Paper III investigates a sigmoidal shape across the gaps. This approach introduces two parameters, defining the position and slope of the transition.

- The energy resolution applied to $E_{\text{out},k}$. Measured spectra indicates that the cameras energy resolution can be described by a linear function of photon energy (Roth et al., 2020). Measurements cannot be directly transferred to the model due to the low-energy tails, but a linear function with adjusted parameters can be used. This approach introduces two parameters to the model.

The first three points are associated with the CIE map calculation, whereas the last point relates to the readout-electronics. Roughly speaking, the diffusion coefficients and the electric and weighting potential parameters primarily affect the lateral shape of the CIE. The mobilities and lifetimes for the charge carriers primarily affect the depth-dependence of the CIE map. It should be noted that the full induced charge for long integration times typically depends on the mobility-lifetime product of a charge carrier, rather than the mobility and lifetime separately, and two quantities are thus not independent (Hecht, 1932; Guerra et al., 2008; Pretorius et al., 2015).

For a given measurement geometry, there may be many sets of parameter values for which the model produces results similar to a physical measurement. In particular, there is a range of possible CIE maps with different depth-dependencies and lateral shapes that could produce spectra with similar low-energy tails. To obtain a model applicable across different measurement set-ups, the model parameters must be tuned towards a variety of experimental set-ups. One idea is to use several radionuclides and collimators, as these factors affect the low-energy tails for measured spectra. Each collimator shields the inter-anode gaps and affects the lateral photon interaction distribution to a varying degree, which allows the lateral shape of the CIE map to be inferred by adjusting the model parameters to match modelled and measured spectra. Similarly, radionuclides with different emission energies produce different photon interaction distributions depth-wise in the crystal, allowing the depth-dependence to be tuned.

It should be noted that all collimators available for the hand-held camera have holes matched to the anode elements of the crystal, which has been critical for this approach of model tuning. Collimators whose holes do not follow the pitch or rectangular arrangement of the anode elements (non-matched collimators) would likely not yield a systematic gap shielding. For full-size gamma cameras, the number of matched collimators at hand may be limited, making this approach to model tuning harder to apply. 3D-printing of matched parallel hole collimators (Gear et al., 2019), not necessarily covering the full detector surface, could address this issue. Another option is to use a scanned collimated photon beam to characterise the detector (Sidambe et al., 2019).

Chapter 5

Summary of papers

Paper I: A method for tumor dosimetry based on hybrid planar-SPECT/CT images and semiautomatic segmentation

In Paper I, a segmentation method, graphical user interface and workflow is developed with the intention to be used for tumour dosimetry calculations based on the gamma camera images acquired in the Iluminet clinical trial. The trial imaging protocol consists of four conjugate-view acquisitions and one SPECT/CT acquisition for each patient and therapy cycle. The large number of images acquired per patient makes operator workload a concern, as does tumour segmentation repeatability. Thus, the inclusion of a semi-automatic segmentation method in the dosimetry workflow was warranted. There is some concern that the time-activity curves estimated for tumours from the conjugate-view images are affected by activity in over- and under-lying activity, and so the accuracy of the method and appropriate tumour selection criteria are investigated. The dosimetry method is found to work well, provided that tumours with major overlapping activity are avoided.

Paper II: Characterisation of a hand-held CZT-based gamma camera for ^{177}Lu imaging

In Paper II, a hand-held CZT-based gamma camera is evaluated. The camera is primarily designed for ^{99m}Tc imaging, but is believed to be valuable for ^{177}Lu imaging as well. The higher photon energies of ^{177}Lu warrants a thorough characterisation, which is achieved mainly following the standard methods of NEMA (2013), with adaptations implemented to overcome limitations of the small camera FOV when necessary. Properties such as energy

resolution, spatial resolution, homogeneity and septal penetration are studied. The camera can be equipped with several collimators, and ^{177}Lu presents three photopeaks suitable for imaging. Therefore, all combinations of collimators and energy windows are investigated to find which configuration works best for imaging. Overall, the camera is found to work well for ^{177}Lu imaging and is believed to be applicable for imaging of smaller tumours or small animals. Imaging at the 113 keV photopeak with a low-energy high-resolution or a medium-energy general-purpose collimator is found to work well.

Paper III: Modelling of a CZT-based gamma camera with application to ^{177}Lu imaging

A Monte Carlo model of a camera system is helpful for obtaining a better understanding of how the system behaves, and can potentially be used to optimise the post-processing methods applied to the acquired images (scatter correction etc.). In Paper III, it is of interest to better understand how the low-energy tails in the energy spectra, a factor present in CZT detectors, affect ^{177}Lu imaging with the hand-held camera. The wide range of relevant energies present in ^{177}Lu spectra (55 keV to 208 keV) motivates the development of a more detailed model of the signal-generation processes in CZT. This is implemented by numerically solving the equations relevant to the signal-generation process and incorporating the solution into a full model of the camera system. To accurately reproduce the camera's behaviour across multiple collimators and energies, an automated model tuning procedure is set-up, matching the model to a set of experimental measurements. The resulting model reproduces the camera response reasonably well, provides insight into its behaviours, and is believed to be a useful tool for future optimisation.

Paper IV: Dosimetric quantities of neuroendocrine tumors over treatment cycles with ^{177}Lu-DOTA-TATE

In Paper IV, the tumour dosimetry method is applied to a larger set of patient images, producing dosimetric data across multiple treatment cycles. The data acquired includes ADs to multiple tumours per patient as well as parameters describing the time-dependent AD-rates for each tumour. The evolution of the ADs and other parameters across treatment cycles is evaluated using a statistical linear mixed-effects model. Grade 1 and grade 2 NETs are treated as separate groups. The model finds that the ADs tends to decrease between treatment cycles, with a more pronounced trend for grade 2 NETs. Applying the model to the dosimetric parameters finds that the decrease in AD is mainly associated with an overall decrease in the magnitude of the activity-concentration curves, while the effective half-life

of the curves changed less over treatment cycles. The findings provide indications for how future treatment protocols and simplified dosimetry methods may be implemented.

Paper v: Feasibility of ^{177}Lu activity quantification using a CZT-based hand-held gamma camera

The hand-held gamma camera has the potential to be useful for dosimetry in RNT by acquiring additional data for time-activity curves, or for other pharmacokinetic studies. In Paper v, the aim is to improve the cameras usefulness further by developing an activity quantification method for it, capable of accounting for attenuation and scatter. As the camera only produces planar images and to avoid the need of a separate imaging modality to estimate source depths, a method for activity quantification is implemented based on the dual-photopeak area method. As ^{177}Lu produces three prominent photopeaks, the new method is called the multiple photopeak method, and contains adaptations to utilise all three peaks. The general approach of the method remains the same as in the dual-photopeak method, and revolves around the fact that each of the photon energies studied have different attenuation coefficients, which allows the source depth to be inferred from the relative count rates measured in the three photopeak windows. The method is studied using both phantom measurements and patient measurements, and is found to be feasible.

Chapter 6

Concluding remarks and future perspectives

Although proponents of individualised treatments in RNT believe in the benefits of dosimetric calculations, many centres employ treatment protocols with fixed administrations (Chiesa et al., 2017). RNT is a comparatively unique form of radiotherapy in that the ADs can in great part be governed by patient-specific factors pertaining to the circulation and uptake of the radiopharmaceutical, which can vary notably between patients. Radiobiological knowledge supports the assumption that tumour and normal organ dosimetry can be used to estimate the tumour-treatment effect and risk of side-effects to organs at risk in RNT. Given the inter-patient variability in uptake, following a protocol with fixed administrations would potentially lead to sub-optimal treatments in some patients, with either incomplete therapeutic effect to tumours or excessive risks for side-effects. Possible reasons for using fixed administrations may be that dosimetric calculations are considered time-consuming and expensive with limited proof of added benefits (Giammarile et al., 2017). The first point can be somewhat alleviated through various simplified dosimetry methods relying on fewer acquired images (Hänscheid et al., 2018; Sundlöv et al., 2018; Jackson et al., 2020), while the latter point may require the comparison of a dosimetry-driven and a fixed treatment protocol in a clinical trial or the establishment of a larger consensus of AD-effect relationship findings. Both of these points mean that there is a value in obtaining more dosimetric data in RNT, both to inform potential choices of simplified dosimetry methods and in the long run to expand the knowledge AD-effect relationships.

Given this context, the overarching goal of the works in this thesis has been to develop methods that facilitates the acquirement of dosimetric data and to add the dosimetric knowledge in RNT. This has in part been realised by developing and investigating a method for tumour dosimetry and then applying it to obtain and study the behaviour of tumour ADs in

[^{177}Lu]Lu-DOTA-TATE PRRT. Additionally a hand-held gamma camera has been characterised and modelled for ^{177}Lu imaging, and an activity quantification method has been developed for it. Thus, the stage is set for using the camera to contribute to the RNT field by applying it to tasks such as pharmacokinetic studies.

The works included in this thesis have presented several possible future topics. A selection of these include

- The tumour-AD data acquired in Paper IV will be used to investigate potential AD-effect relationships in [^{177}Lu]Lu-DOTA-TATE PRRT in a future study.

- The CZT camera model developed in Paper III is not limited to the simulation of the hand-held camera, but may be applied and tuned other CZT-based gamma cameras as well.

- The hand-held gamma camera may be applied to more patients undergoing ^{177}Lu-based treatments to gain more knowledge on pharmacokinetic behaviours. This includes for instance the study of the activity-uptake during and shortly after the administration of the radiopharmaceutical. The camera may also be used to acquire an overall greater set of data over more time-points, something that may be considered cumbersome with a conventional gamma camera.

- The activity quantification method studied in Paper V may be developed further. Possible directions induces its application to conventional gamma cameras, extending it into a pixel-based method, or combining it with stereoscopic imaging.

Acknowledgements

There are many people to whom I would like to express my gratitude for these years as a PhD student. All your support, lessons, discussions and kindness is immensely appreciated.

- To my main supervisor, Katarina Sjögreen Gleisner

- To my supervisor, Erik Larsson

- To my closest collaborators, Johan Gustafsson and Michael Ljungberg

- To my co-authors

- To all the people in the Nuclear Medicine Group

- To all the people at the Medical Radiation Physics Department

- To my parents and my brother

Appendix A

Adjoint method for CIE calculation

It is possible to map out the detector response with equations 2.10–2.12, but repeatedly solving the transport equations for each starting point $(\vec{r}_0)$ of interest is computationally expensive. Prettyman (1999) notes that equations 2.10 and 2.11 involve linear operators, which allows for an adjoint problem to be formed and solved instead. Practically, adjoint charge concentrations n^+ and p^+ are introduced, which are related to the regular charge concentrations counterparts n and p. The adjoint concentrations and their transport equations are defined to satisfy certain conditions based on the regular charge transport. With charge transport defined as in equations 2.10 and 2.11, the equations for n^+ and p^+ become

$$\frac{\partial n^+}{\partial t} = \mu_n \nabla\varphi \cdot \nabla n^+ + \nabla \cdot (D_n \nabla n^+) + G_n^+ - n^+/\tau_n, \tag{A.1}$$

$$\frac{\partial p^+}{\partial t} = -\mu_p \nabla\varphi \cdot \nabla p^+ + \nabla \cdot (D_p \nabla p^+) + G_p^+ - p^+/\tau_p. \tag{A.2}$$

These equations are similar to equations 2.10 and 2.11, with the major difference being that adjoint concentrations move in the opposite direction along the electric field compared to their physical counterparts n and p. The advantage of the adjoint method arises when the generation terms are defined as $G_n^+ = \mu_n \nabla\varphi \cdot \nabla\varphi_k$ and $G_p^+ = \mu_p \nabla\varphi \cdot \nabla\varphi_k$, in which case the adjoint charge concentrations can be shown to be equal to the CIEs of the corresponding charge carriers (Prettyman, 1999; Mathy et al., 2004). I.e. $n^+(\vec{r}, t) = \eta_{n,k}(\vec{r}, t)$ and $p^+(\vec{r}, t) = \eta_{p,k}(\vec{r}, t)$. More details on the mathematics behind the adjoint method are given in Mathy et al. (2004).

This means that $\eta_{n,k}(\vec{r}, t)$ and $\eta_{p,k}(\vec{r}, t)$ can be determined for all starting interaction positions simultaneously by solving equations A.1 and A.2 once, rather than repeatedly solving equations 2.10 and 2.11 in combination with equation 2.12 for all possible $\vec{r}_0$.

Appendix B

A numerical solution to the signal-generation equations

Differential equations such as those in equations 2.5, 2.10 and 2.11 can be solved analytically for a limited number of situations, e.g. for simple detector geometries or with charge motion restricted to one dimension. More general detector models require approximate numerical methods to solve the equations. There are several methods to solve such equations, one of which is the finite difference method, which has been used in this thesis (Press et al., 2007; Kuzmin, 2010; Kajishima and Taira, 2017).

1   Electric and weighting potential

In the finite difference method, the equation is considered on a grid containing a discrete set of points. Using equation 2.5 as an example, the quantities φ and ρ can be represented by their values on a Cartesian grid x_i, y_j, z_k given by

$$x_i = x_0 + i \cdot \Delta, \quad i = 0, 1, \ldots N_x - 1, \tag{B.1}$$

$$y_j = y_0 + j \cdot \Delta, \quad j = 0, 1, \ldots N_y - 1, \tag{B.2}$$

$$z_k = z_0 + k \cdot \Delta, \quad k = 0, 1, \ldots N_z - 1, \tag{B.3}$$

where Δ is a spatial step length.

In Cartesian coordinates, equation 2.5 can be written as

$$\frac{\partial^2 \varphi}{\partial x^2} + \frac{\partial^2 \varphi}{\partial y^2} + \frac{\partial^2 \varphi}{\partial z^2} = \frac{\rho}{\varepsilon}. \tag{B.4}$$

In the finite difference method, these derivatives are approximated by differences between nearby points. For example

$$\left(\frac{\partial^2 \varphi}{\partial x^2} + \frac{\partial^2 \varphi}{\partial y^2} + \frac{\partial^2 \varphi}{\partial z^2}\right)\Bigg|_{x_i, y_j, z_k} \simeq \frac{\varphi_{i-1,j,k} - 2\varphi_{i,j,k} + \varphi_{i+1,j,k}}{\Delta^2}$$

$$+ \frac{\varphi_{i,j-1,k} - 2\varphi_{i,j,k} + \varphi_{i,j+1,k}}{\Delta^2} \qquad \text{(B.5)}$$

$$+ \frac{\varphi_{i,j,k-1} - 2\varphi_{i,j,k} + \varphi_{i,j,k+1}}{\Delta^2}.$$

where the notation $\varphi(x_i, y_j, z_k) = \varphi_{i,j,k}$ has been used. The following linear equation system can be formed by combining equations B.4 and B.5

$$\varphi_{i-1,j,k} + \varphi_{i+1,j,k} + \varphi_{i,j-1,k} + \varphi_{i,j+1,k} + \varphi_{i,j,k-1} + \varphi_{i,j,k+1} - 6\varphi_{i,j,k}$$
$$= \Delta^2 \rho_{i,j,k}/\varepsilon. \qquad \text{(B.6)}$$

Special attention needs to be given to points at the edges of the grids (e.g. where $i = 0$ or $i = N_x - 1$). For such points, there are missing neighbours in one or more directions. For instance, at grid points where $k = 0$, the neighbouring point $\varphi_{i,j,k-1}$ does not exist on the grid. How such points are dealt with depends on the boundary conditions for the equation. For instance, if a boundary condition states that φ has a specific value on an electrode (e.g. –600 V on the cathode), then $\varphi_{i,j,k-1}$ has a known value and can be moved to the right-hand side of equation B.6. Alternatively, if a boundary condition states that $\partial\varphi/\partial z$ is known on the boundary, then the difference $(\varphi_{i,j,k} - \varphi_{i,j,k-1})$ (which is proportional to the derivative) can be moved to the right-hand side.

The $N = N_x \cdot N_y \cdot N_z$ grid points gives rise to a system with N linear equations that needs to be solved simultaneously. Methods for doing so exist when the equation system is expressed in a matrix multiplication form. To obtain a system of linear equations on this form, φ needs to be reformed from a $N_x \times N_y \times N_z$ array to an N-element vector. This can be done by defining the linear index $l = k + j \cdot N_z + i \cdot N_z \cdot N_y$, which allows equation B.6 to be written as

$$\varphi_{l-N_z N_y} + \varphi_{l+N_z N_y} + \varphi_{l-N_z} + \varphi_{l+N_z} + \varphi_{l-1} + \varphi_{l+1} - 6\varphi_l = \Delta^2 \rho_l/\varepsilon, \qquad \text{(B.7)}$$

where the notation $\varphi_l = \varphi_{i,j,k}$ has been used. The linear equation system that equation B.7 gives can now be expressed in the form of a matrix multiplication

$$\mathbf{M} \cdot \varphi = \mathbf{b}, \qquad \text{(B.8)}$$

where $\mathbf{b}$ corresponds to the right-hand side of equation B.7 and $\mathbf{M} \cdot \varphi$ corresponds to the left-hand side. The $N \times N$ matrix $\mathbf{M}$ describes how a centre point φ_l and its neighbours $\varphi_{l-1}, \varphi_{l+1}, \dots$ relate to each other in equation B.7. Since φ_l only relates to its six nearest

neighbours, the matrix $\mathbf{M}$ will be sparse and contain seven diagonals with non-zero values. Solving matrix equations such as B.8 with large sparse matrices is the subject of many algorithms. The solution to equation B.8 gives the values of $\varphi(x_i, y_j, z_k)$, which forms the numerical solution to equation 2.5.

2   Charge transport

Equation 2.5 is a so-called boundary value problem, in which a static solution that satisfies a condition is determined. Equations 2.10, 2.11, A.1 and A.2, on the other hand, are initial value problems, in which a quantity is evolved over time given a starting situation. Such problems can be solved with a finite difference methodology similar to that of boundary value problems, but special considerations regarding temporal and spatial discretisation step sizes and the numerical approximations for the derivatives may be necessary to ensure stability and accuracy of the result.

Equation A.1 will be used as an example in this section, but equations 2.10, 2.11 and A.2 can be treated similarly. Using the same general finite difference methodology as for the electric potential, a discrete spatial grid is defined, as well as a temporal grid. The value of the adjoint electron concentration $n^+(x, y, z, t)$ is now considered on the grid x_i, y_j, z_k, t_m. As before, it is possible to convert the spatial indices i, j, k to a linear index l. The temporal index m is kept separate from the spatial index. The spatial derivatives in equation A.1 can be approximated using finite differences in a manner similar to what was done with equation 2.5. In this way, a system of equations can be derived from equation A.1 and expressed as the matrix multiplication

$$\frac{\partial n^+}{\partial t} = (\mathbf{C} + \mathbf{D} - \mathbf{R}) \cdot n^+ + G, \tag{B.9}$$

where n^+ is the vector containing the linearly arranged values $n_l^+ = n_{i,j,k}^+$ and $\mathbf{C}, \mathbf{D}, \mathbf{R}$ and G are finite difference approximations for the following terms:

$$\begin{aligned}
\mu_n \nabla \varphi \nabla n^+ &\sim \mathbf{C} \cdot n^+ \quad \text{(convection)} \\
\nabla D_n \nabla n^+ &\sim \mathbf{D} \cdot n^+ \quad \text{(diffusion)} \\
n^+/\tau_n &\sim \mathbf{R} \cdot n^+ \quad \text{(trapping)} \\
G_n^+ &\sim G \quad \text{(charge generation).}
\end{aligned}$$

Care needs to be taken in how the spatial and temporal derivatives are calculated to obtain an accurate and stable result in equation B.9. Furthermore, the convection and diffusion terms may each require different strategies. These are best illustrated in one dimension.

In one dimension, the convection equation can be rewritten as

$$\frac{\partial n^+}{\partial t} = -v \cdot \frac{\partial n^+}{\partial x}.$$

Using the convention $n^+\left(x_i, t_m\right) = n_{i,m}^+$, the derivatives can be approximated as

$$\frac{n_{i,m+1}^+ - n_{i,m}^+}{\Delta t} = -v \cdot \frac{n_{i+1,m}^+ - n_{i-1,m}^+}{2\Delta x}.$$

This differencing scheme is called *forward time centred space*, and has the advantage of allowing n^+ at time t_{m+1} to be calculated only from values of n^+ at t_m. This method should not be used, however, as the resulting n^+ is unstable when evolved over time. Furthermore, the value of n^+ at a point x_i will affect the values at points x_{i-1} and x_{i+1} at the next time step, regardless of the sign of v (direction of motion). In reality, if $v > 0$, then only the x_{i+1} point should be affected by charge located in x_i. This transportation error can be corrected through an upwind differencing scheme, such as

$$\frac{n_{i,m+1}^+ - n_{i,m}^+}{\Delta t} = -v \begin{cases} \frac{n_{i,m}^+ - n_{i-1,m}^+}{\Delta x} & v > 0 \\ \frac{n_{i+1,m}^+ - n_{i,m}^+}{\Delta x} & v \le 0 \end{cases},$$

which in a sense has better transport properties, and additionally is stable under the condition that $\frac{|v|\Delta t}{\Delta x} \le 1$. An upwind differencing scheme can thus be implemented in the $\mathbf{C}$ matrix of equation B.9 in order to improve the transport properties and obtain some stability.

There are further considerations to be made for the differencing in time. The method used in the *forward time centred space* scheme is known as the forward Euler method, which is an explicit method in which n_{m+1}^+ is calculated only from values in n_m^+. The forward Euler method for equation B.9 can be written as

$$\frac{n_{m+1}^+ - n_m^+}{\Delta t} = (\mathbf{C} + \mathbf{D} - \mathbf{R}) \cdot n_m^+ + G. \tag{B.10}$$

There is also a corresponding backwards Euler method, in which n_m^+ is replaced by n_{m+1}^+ on the right-hand side of the equation:

$$\frac{n_{m+1}^+ - n_m^+}{\Delta t} = (\mathbf{C} + \mathbf{D} - \mathbf{R}) \cdot n_{m+1}^+ + G. \tag{B.11}$$

This is an implicit method, in which n_{m+1}^+ cannot be calculated directly from n_m^+, but must instead be found as a solution to a system of equations. Equation B.11 can be rearranged as

$$[\mathbf{I} - (\mathbf{C} + \mathbf{D} - \mathbf{R}) \cdot \Delta t] \cdot n_{m+1}^+ = n_m^+ + G \cdot \Delta t, \tag{B.12}$$

where $\mathbf{I}$ is an identity matrix. This equation can be solved similarly to equation B.8. The implicit method has some advantages over the explicit methods as the method is stable for diffusion equations for all temporal step sizes Δt (Press et al., 2007; Kajishima and Taira, 2017).

Evolving n^+ over time through a differencing scheme gives the CIE for electrons, since G_n^+ was been chosen such that $n^+(\vec{r}, t) = \eta_{n,k}(\vec{r}, t)$. Since all electrons will eventually either leave the detector volume or become trapped, there should be a point in time when the electron concentration reaches zero ($n(\vec{r}, t) = 0$), at which point $\eta_{n,k}(\vec{r}, t)$ would no longer change over time. At this point, the time derivative of n^+ should consequently also be zero. This state can be reached by evolving n^+ over a long period using equation B.9, but another possibility is to set $\frac{\partial n^+}{\partial t} = 0$ in equation B.9, which yields the boundary value problem

$$(\mathbf{C} + \mathbf{D} - \mathbf{R}) \cdot n^+ = -G, \tag{B.13}$$

whose solution should correspond to something akin to $\lim_{t \to \infty} n^+(\vec{r}, t)$.

References

Abe, A., Takahashi, N., Lee, J., Oka, T., Shizukuishi, K., Kikuchi, T., Inoue, T., Jimbo, M., Ryuo, H. and Bickel, C. (2003). Performance evaluation of a hand-held, semiconductor (CdZnTe)-based gamma camera, *European Journal of Nuclear Medicine and Molecular Imaging* **30**(6): 805–811.

Andersson, M., Johansson, L., Eckerman, K. and Mattsson, S. (2017). IDAC-dose 2.1, an internal dosimetry program for diagnostic nuclear medicine based on the ICRP adult reference voxel phantoms, *EJNMMI Research* **7**(1): 88.

Anger, H. O. (1958). Scintillation camera, *Review of Scientific Instruments* **29**(1): 27–33.

Barone, R., Borson-Chazot, F., Valkema, R., Walrand, S., Chauvin, F., Gogou, L., Kvols, L. K., Krenning, E. P., Jamar, F. and Pauwels, S. (2005). Patient-specific dosimetry in predicting renal toxicity with 90Y-DOTATOC: Relevance of kidney volume and dose rate in finding a dose–effect relationship, *Journal of Nuclear Medicine* **46**(1 suppl): 99S–106S.

Barrett, H. H., Eskin, J. D. and Barber, H. B. (1995). Charge transport in arrays of semiconductor gamma-ray detectors, *Physical Review Letters* **75**: 156–159.

Bergsma, H., Konijnenberg, M. W., Kam, B. L. R., Teunissen, J. J. M., Kooij, P. P., de Herder, W. W., Franssen, G. J. H., van Eijck, C. H. J., Krenning, E. P. and Kwekkeboom, D. J. (2016). Subacute haematotoxicity after PRRT with 177Lu-DOTA-octreotate: prognostic factors, incidence and course, *European Journal of Nuclear Medicine and Molecular Imaging* **43**(3): 453–463.

Blaire, T., Bailliez, A., Bouallegue, F. B., Bellevre, D., Agostini, D. and Manrique, A. (2016). Left ventricular function assessment using 123I/99mTc dual-isotope acquisition with two semi-conductor cadmium–zinc–telluride (CZT) cameras: a gated cardiac phantom study, *EJNMMI Physics* **3**(1): 27.

Bodei, L., Cremonesi, M., Ferrari, M., Pacifici, M., Grana, C. M., Bartolomei, M., Baio, S. M., Sansovini, M. and Paganelli, G. (2008). Long-term evaluation of renal tox-

icity after peptide receptor radionuclide therapy with 90Y-DOTATOC and 177Lu-DOTATATE: the role of associated risk factors, *European Journal of Nuclear Medicine and Molecular Imaging* **35**(10): 1847–1856.

Bodei, L., Cremonesi, M., Grana, C. M., Fazio, N., Iodice, S., Baio, S. M., Bartolomei, M., Lombardo, D., Ferrari, M. E., Sansovini, M., Chinol, M. and Paganelli, G. (2011). Peptide receptor radionuclide therapy with 177Lu-DOTATATE: the IEO phase I-II study, *European Journal of Nuclear Medicine and Molecular Imaging* **38**(12): 2125–2135.

Bodei, L., Mueller-Brand, J., Baum, R. P., Pavel, M. E., Hörsch, D., O'Dorisio, M. S., O'Dorisio, T. M., Howe, J. R., Cremonesi, M., Kwekkeboom, D. J. and Zaknun, J. J. (2013). The joint IAEA, EANM, and SNMMI practical guidance on peptide receptor radionuclide therapy (PRRNT) in neuroendocrine tumours, *European Journal of Nuclear Medicine and Molecular Imaging* **40**(5): 800–816. Note: author order and spelling have been corrected as per published erratum (Bodei et al., 2014).

Bodei, L., Mueller-Brand, J., Baum, R. P., Pavel, M. E., Hörsch, D., O'Dorisio, M. S., O'Dorisio, T. M., Howe, J. R., Cremonesi, M., Kwekkeboom, D. J. and Zaknun, J. J. (2014). Erratum to: The joint IAEA, EANM, and SNMMI practical guidance on peptide receptor radionuclide therapy (PRRNT) in neuroendocrine tumours, *European Journal of Nuclear Medicine and Molecular Imaging* **41**: 584.

Bolch, W. E., Eckerman, K. F., Sgouros, G. and Thomas, S. R. (2009). MIRD pamphlet no. 21: A generalized schema for radiopharmaceutical dosimetry—standardization of nomenclature, *Journal of Nuclear Medicine* **50**(3): 477–484.

Bolotnikov, A. E., Camarda, G. C., Wright, G. W. and James, R. B. (2005). Factors limiting the performance of CdZnTe detectors, *IEEE Transactions on Nuclear Science* **52**(3): 589–598.

Bolotnikov, A. E., Cook, W. R., Harrison, F. A., Wong, A. S., Schindler, S. M. and Eichelberger, A. C. (1999). Charge loss between contacts of CdZnTe pixel detectors, *Nuclear Instruments and Methods in Physics Research Section A: Accelerators, Spectrometers, Detectors and Associated Equipment* **432**(2): 326 – 331.

Breen, S. L., Publicover, J., Silva, S. D., Pond, G., Brock, K., O'Sullivan, B., Cummings, B., Dawson, L., Keller, A., Kim, J., Ringash, J., Yu, E., Hendler, A. and Waldron, J. (2007). Intraobserver and interobserver variability in GTV delineation on FDG-PET-CT images of head and neck cancers, *International Journal of Radiation Oncology, Biology, Physics* **68**(3): 763 – 770.

Brolin, G., Gustafsson, J., Ljungberg, M. and Sjögreen Gleisner, K. (2015). Pharmacokinetic digital phantoms for accuracy assessment of image-based dosimetry in 177Lu-DOTATATE peptide receptor radionuclide therapy, *Physics in Medicine and Biology* **60**(15): 6131–6149.

Castoldi, A., Gatti, E. and Rehak, P. (1996). Three-dimensional analytical solution of the Laplace equation suitable for semiconductor detector design, *IEEE Transactions on Nuclear Science* **43**(1): 256–265.

Chatal, J.-F. and Hoefnagel, C. A. (1999). Radionuclide therapy, *The Lancet* **354**(9182): 931–935.

Chauvin, M., Borys, D., Botta, F., Bzowski, P., Dabin, J., Denis-Bacelar, A. M., Desbrée, A., Falzone, N., Lee, B. Q., Mairani, A., Malaroda, A., Mathieu, G., McKay, E., Mora-Ramirez, E., Robinson, A. P., Sarrut, D., Struelens, L., Gil, A. V. and Bardiès, M. (2020). Opendose: Open-access resource for nuclear medicine dosimetry, *Journal of Nuclear Medicine* **61**(10): 1514–1519.

Chiesa, C., Sjogreen Gleisner, K., Flux, G., Gear, J., Walrand, S., Bacher, K., Eberlein, U., Visser, E. P., Chouin, N., Ljungberg, M., Bardiès, M., Lassmann, M., Strigari, L. and Konijnenberg, M. W. (2017). The conflict between treatment optimization and registration of radiopharmaceuticals with fixed activity posology in oncological nuclear medicine therapy, *European Journal of Nuclear Medicine and Molecular Imaging* **44**(11): 1783–1786.

Cives, M. and Strosberg, J. (2017). Radionuclide therapy for neuroendocrine tumors, *Current Oncology Reports* **19**(2): 9.

d'Aillon, E. G., Gentet, M. C., Montemont, G., Rustique, J. and Verger, L. (2005). Simulation and experimental results on monolithic CdZnTe gamma-ray detectors, *IEEE Transactions on Nuclear Science* **52**(6): 3096–3102.

d'Aillon, E. G., Tabary, J., Glière, A. and Verger, L. (2006). Charge sharing on monolithic CdZnTe gamma-ray detectors: A simulation study, *Nuclear Instruments and Methods in Physics Research Section A: Accelerators, Spectrometers, Detectors and Associated Equipment* **563**(1): 124 – 127. Proceedings of the 7th International Workshop on Radiation Imaging Detectors.

Dash, A., Chakraborty, S., Pillai, M. R. A. and Knapp, F. F. R. (2015). Peptide receptor radionuclide therapy: An overview, *Cancer Biotherapy and Radiopharmaceuticals* **30**(2): 47–71. PMID: 25710506.

Del Prete, M., Buteau, F.-A., Arsenault, F., Saighi, N., Bouchard, L.-O., Beaulieu, A. and Beauregard, J.-M. (2019). Personalized 177Lu-octreotate peptide receptor radionuclide therapy of neuroendocrine tumours: initial results from the P-PRRT trial, *European Journal of Nuclear Medicine and Molecular Imaging* **46**(3): 728–742.

Del Prete, M., Buteau, F.-A. and Beauregard, J.-M. (2017). Personalized 177Lu-octreotate peptide receptor radionuclide therapy of neuroendocrine tumours: a simulation study, *European Journal of Nuclear Medicine and Molecular Imaging* **44**(9): 1490–1500.

Denzler, J. and Niemann, H. (1999). Active rays: Polar-transformed active contours for real-time contour tracking, *Real-Time Imaging* **5**(3): 203–213.

Dewaraja, Y. K., Frey, E. C., Sgouros, G., Brill, A. B., Roberson, P., Zanzonico, P. B. and Ljungberg, M. (2012). MIRD pamphlet no. 23: Quantitative SPECT for patient-specific 3-dimensional dosimetry in internal radionuclide therapy, *Journal of Nuclear Medicine* **53**(8): 1310–1325.

Einstein, A. (1905). Über die von der molekularkinetischen theorie der wärme geforderte bewegung von in ruhenden flüssigkeiten suspendierten teilchen, *Annalen der Physik* **322**(8): 549–560.

Eisen, Y., Mardor, I., Shor, A., Baum, Z., Bar, D., Feldman, G., Cohen, H., Issac, E., Haham-Zada, R., Blitz, S., Cohen, Y., Glick, B., Falk, R., Roudebush, S. and Blevis, I. (2002). NUCAM3-a gamma camera based on segmented monolithic CdZnTe detectors, *IEEE Transactions on Nuclear Science* **49**(4): 1728–1732.

Eskin, J. D., Barrett, H. H. and Barber, H. B. (1999). Signals induced in semiconductor gamma-ray imaging detectors, *Journal of Applied Physics* **85**(2): 647–659.

Fan, P., Hutton, B. F., Holstensson, M., Ljungberg, M., Hendrik Pretorius, P., Prasad, R., Ma, T., Liu, Y., Wang, S., Thorn, S. L., Stacy, M. R., Sinusas, A. J. and Liu, C. (2015). Scatter and crosstalk corrections for 99mTc/123I dual-radionuclide imaging using a CZT SPECT system with pinhole collimators, *Medical Physics* **42**(12): 6895–6911.

Fiederle, M., Sowinska, M., Fauler, A., Konrath, J. ., Benz, K. W. and Siffert, P. (2003). Search of a characterisation methodology of CdTe/CZT wafers for imaging, *2003 IEEE Nuclear Science Symposium. Conference Record (IEEE Cat. No.03CH37515)*, Vol. 5, pp. 3331–3335b.

Flux, G. D., Sjogreen Gleisner, K., Chiesa, C., Lassmann, M., Chouin, N., Gear, J., Bardiès, M., Walrand, S., Bacher, K., Eberlein, U., Ljungberg, M., Strigari, L., Visser, E. and Konijnenberg, M. W. (2018). From fixed activities to personalized treatments in radionuclide therapy: lost in translation?, *European Journal of Nuclear Medicine and Molecular Imaging* **45**(1): 152–154.

Forrer, F., Krenning, E. P., Kooij, P. P., Bernard, B. F., Konijnenberg, M., Bakker, W. H., Teunissen, J. J. M., de Jong, M., van Lom, K., de Herder, W. W. and Kwekkeboom, D. J. (2009). Bone marrow dosimetry in peptide receptor radionuclide therapy with [177Lu-DOTA0,Tyr3]octreotate, *European Journal of Nuclear Medicine and Molecular Imaging* **36**(7): 1138–1146.

Frey, E. C. and Tsui, B. M. W. (1993). A practical method for incorporating scatter in a projector-backprojector for accurate scatter compensation in SPECT, *IEEE Transactions on Nuclear Science* **40**(4): 1107–1116.

Frey, E. C. and Tsui, B. M. W. (1996). A new method for modeling the spatially-variant, object-dependent scatter response function in SPECT, *1996 IEEE Nuclear Science Symposium. Conference Record*, Vol. 2, pp. 1082–1086 vol.2.

Garske-Román, U., Sandström, M., Fröss Baron, K., Lundin, L., Hellman, P., Welin, S., Johansson, S., Khan, T., Lundqvist, H., Eriksson, B., Sundin, A. and Granberg, D. (2018). Prospective observational study of 177Lu-DOTA-octreotate therapy in 200 patients with advanced metastasized neuroendocrine tumours (NETs): feasibility and impact of a dosimetry-guided study protocol on outcome and toxicity, *European Journal of Nuclear Medicine and Molecular Imaging* **45**(6): 970–988.

Gear, J. I., Taprogge, J., White, O. and Flux, G. D. (2019). Characterisation of the attenuation properties of 3D-printed tungsten for use in gamma camera collimation, *EJNMMI Physics* **6**(1).

Giammarile, F., Muylle, K., Delgado Bolton, R., Kunikowska, J., Haberkorn, U. and Oyen, W. (2017). Dosimetry in clinical radionuclide therapy: the devil is in the detail, *European Journal of Nuclear Medicine and Molecular Imaging* **44**(12): 1–3.

Guerra, P., Santos, A. and Darambara, D. (2008). Development of a simplified simulation model for performance characterization of a pixellated CdZnTe multimodality imaging system, *Physics in Medicine and Biology* **53**(4): 1099–1113.

Gupta, S. K., Singla, S. and Bal, C. (2012). Renal and hematological toxicity in patients of neuroendocrine tumors after peptide receptor radionuclide therapy with 177Lu-DOTATATE, *Cancer Biotherapy and Radiopharmaceuticals* **27**(9): 593–599.

Gustafsson, J., Brolin, G., Cox, M., Ljungberg, M., Johansson, L. and Sjögreen Gleisner, K. (2015). Uncertainty propagation for SPECT/CT-based renal dosimetry in 177Lu peptide receptor radionuclide therapy, *Physics in Medicine and Biology* **60**(21): 8329–8346.

Gustafsson, J., Sundlöv, A. and Sjögreen Gleisner, K. (2017). SPECT image segmentation for estimation of tumour volume and activity concentration in 177Lu-DOTATATE radionuclide therapy, *EJNMMI Research* **7**(1).

Hamel, L.-A. and Paquet, S. (1996). Charge transport and signal generation in CdTe pixel detectors, *Nuclear Instruments and Methods in Physics Research Section A: Accelerators, Spectrometers, Detectors and Associated Equipment* **380**(1): 238–240.

He, Z. (1995). Potential distribution within semiconductor detectors using coplanar electrodes, *Nuclear Instruments & Methods A* **365**(2-3): 572–575.

He, Z. (2001). Review of the Shockley–Ramo theorem and its application in semiconductor gamma-ray detectors, *Nuclear Instruments and Methods in Physics Research Section A: Accelerators, Spectrometers, Detectors and Associated Equipment* **463**(1): 250 – 267.

Hecht, K. (1932). Zum mechanismus des lichtelektrischen primärstromes in isolierenden kristallen, *Zeitschrift für Physik* **77**(3): 235–245.

Heller, S. and Zanzonico, P. (2011). Nuclear probes and intraoperative gamma cameras, *Seminars in Nuclear Medicine* **41**(3): 166 – 181.

Hänscheid, H., Lapa, C., Buck, A. K., Lassmann, M. and Werner, R. A. (2018). Dose mapping after endoradiotherapy with 177Lu-DOTATATE/DOTATOC by a single measurement after 4 days, *Journal of Nuclear Medicine* **59**(1): 75–81.

Holstensson, M., Erlandsson, K., Poludniowski, G., Ben-Haim, S. and Hutton, B. F. (2015). Model-based correction for scatter and tailing effects in simultaneous 99mTc and123I imaging for a CdZnTe cardiac SPECT camera, *Physics in Medicine and Biology* **60**(8): 3045–3063.

Ilan, E., Sandström, M., Wassberg, C., Sundin, A., Garske–Román, U., Eriksson, B., Granberg, D. and Lubberink, M. (2015). Dose response of pancreatic neuroendocrine tumors treated with peptide receptor radionuclide therapy using 177Lu-DOTATATE, *Journal of Nuclear Medicine* **56**(2): 177–182.

Jackson, P. A., Hofman, M. S., Hicks, R. J., Scalzo, M. and Violet, J. (2020). Radiation dosimetry in 177Lu-PSMA-617 therapy using a single posttreatment SPECT/CT scan: A novel methodology to generate time- and tissue-specific dose factors, *Journal of Nuclear Medicine* **61**(7): 1030–1036.

Jahn, U., Ilan, E., Sandström, M., Lubberink, M., Garske-Román, U. and Sundin, A. (2021). Peptide receptor radionuclide therapy (PRRT) with 177Lu-DOTATATE; differences in tumor dosimetry, vascularity and lesion metrics in pancreatic and small intestinal neuroendocrine neoplasms, *Cancers* **13**(5).

James, R. B., Brunett, B., Heffelfinger, J., Van Scyoc, J., Lund, J., Doty, F. P., Lingren, C. L., Olsen, R., Cross, E., Hermon, H., Yoon, H., Hilton, N., Schieber, M., Lee, E. Y., Toney, J., Schlesinger, T. E., Goorsky, M., Yao, W., Chen, H. and Burger, A. (1998). Material properties of large-volume cadmium zinc telluride crystals and their relationship to nuclear detector performance, *Journal of Electronic Materials* **27**(6): 788–799.

Jan, S., Santin, G., Strul, D., Staelens, S., Assié, K., Autret, D., Avner, S., Barbier, R., Bardiès, M., Bloomfield, P. M., Brasse, D., Breton, V., Bruyndonckx, P., Buvat, I., Chatziioannou, A. F., Choi, Y., Chung, Y. H., Comtat, C., Donnarieix, D., Ferrer,

L., Glick, S. J., Groiselle, C. J., Guez, D., Honore, P.-F., Kerhoas-Cavata, S., Kirov, A. S., Kohli, V., Koole, M., Krieguer, M., van der Laan, D. J., Lamare, F., Largeron, G., Lartizien, C., Lazaro, D., Maas, M. C., Maigne, L., Mayet, F., Melot, F., Merheb, C., Pennacchio, E., Perez, J., Pietrzyk, U., Rannou, F. R., Rey, M., Schaart, D. R., Schmidtlein, C. R., Simon, L., Song, T. Y., Vieira, J.-M., Visvikis, D., de Walle, R. V., Wieërs, E. and Morel, C. (2004). GATE: a simulation toolkit for PET and SPECT, *Physics in Medicine and Biology* **49**(19): 4543–4561.

Jung, I., Krawczynski, H., Komarov, S. and Sobotka, L. (2006). Simulation studies of CZT detectors as gamma-ray calorimeter, *Astroparticle Physics* **26**(2): 119–128.

Kacperski, K., Erlandsson, K., Ben-Haim, S. and Hutton, B. F. (2011). Iterative deconvolution of simultaneous 99mTc and 201Tl projection data measured on a CdZnTe-based cardiac SPECT scanner, *Physics in Medicine and Biology* **56**(5): 1397–1414.

Kajishima, T. and Taira, K. (2017). *Finite-Difference Discretization of the Advection-Diffusion Equation*, Springer International Publishing, Cham, pp. 23–72.

Kass, M., Witkin, A. and Terzopoulos, D. (1988). Snakes: Active contour models, *International Journal of Computer Vision* **1**(4): 321–331.

Kellett, M. A. and Bersillon, O. (2017). The decay data evaluation project (DDEP) and the JEFF-3.3 radioactive decay data library: Combining international collaborative efforts on evaluated decay data, *European Physical Journal Web of Conferences*, Vol. 146 of *European Physical Journal Web of Conferences*, p. 02009.

Kerrou, K., Pitre, S., Coutant, C., Rouzier, R., Ancel, P.-Y., Lebeaux, C., Huchet, V., Montravers, F., Pascal, O., Duval, M.-A., Lefebvre, F., Menard, L., Uzan, S., Charon, Y. and Barranger, E. (2011). The usefulness of a preoperative compact imager, a hand-held γ-camera for breast cancer sentinel node biopsy: Final results of a prospective double-blind, clinical study, *Journal of Nuclear Medicine* **52**(9): 1346–1353.

Kim, J. C., Kaye, W. R., Yang, H., Brown, C. R. and He, Z. (2013). Improvement of sub-pixel position sensing in nonuniform large-volume pixelated CdZnTe crystals, *IEEE Transactions on Nuclear Science* **60**(2): 1201–1207.

Knoll, G. F. (2010). *Radiation detection and measurement*, fourth edn, John Wiley & Sons.

Knoll, P., Mirzaei, S., Schwenkenbecher, K. and Barthel, T. (2015). Performance evaluation of a solid-state detector based handheld gamma camera system, *Frontiers in Biomedical Technologies* **1**(1): 61–67.

Kotoch, T. B., Nandi, A., Debnath, D., Malkar, J. P., Rao, A. R., Hingar, M. K., Madhav, V. P., Sreekumar, S. and Chakrabarti, S. K. (2011). Instruments of RT-2 experiment

onboard CORONAS-PHOTON and their test and evaluation II: RT-2/CZT payload, *Experimental Astronomy* **29**(1): 27–54.

Krane, K. S. and Halliday, D. (1987). *Introductory nuclear physics*, third edn, John Wiley & Sons.

Kuzmin, D. (2010). *A guide to numerical methods for transport equations*, Friedrich-Alexander-Universität Erlangen-Nürnberg.

Ljungberg, M., Celler, A., Konijnenberg, M. W., Eckerman, K. F., Dewaraja, Y. K. and Sjögreen-Gleisner, K. (2016). MIRD pamphlet no. 26: Joint EANM/MIRD guidelines for quantitative 177Lu SPECT applied for dosimetry of radiopharmaceutical therapy, *Journal of Nuclear Medicine* **57**(1): 151–162.

Ljungberg, M., Larsson, A. and Johansson, L. (2005). A new collimator simulation in SIMIND based on the delta-scattering technique, *IEEE Transactions on Nuclear Science* **52**(5): 1370–1375.

Ljungberg, M. and Sjögreen Gleisner, K. (2011). The accuracy of absorbed dose estimates in tumours determined by quantitative SPECT: A monte carlo study, *Acta Oncologica* **50**(6): 981–989.

Ljungberg, M. and Strand, S.-E. (1989). A Monte Carlo program for the simulation of scintillation camera characteristics, *Computer Methods and Programs in Biomedicine* **29**(4): 257–272.

Loevinger, R. and Berman, M. (1968). A formalism for calculation of absorbed dose from radionuclides, *Physics in Medicine and Biology* **13**(2): 205–217.

Mardor, I., Shor, A. and Eisen, Y. (2001). Edge and corner effects on spectra of segmented CdZnTe detectors, *IEEE Transactions on Nuclear Science* **48**(4): 1033–1040.

Mathy, F., Gliere, A., d'Aillon, E. G., Masse, P., Picone, M., Tabary, J. and Verger, L. (2004). A three-dimensional model of CdZnTe gamma-ray detector and its experimental validation, *IEEE Transactions on Nuclear Science* **51**(5): 2419–2426.

Mayer, M., Boykin, D. V., Cherry, M. L., Courville, J. F., Doty, F. P., Drake, A., Guzik, T. G., Hamel, L. A., Larson, K., Macri, J. R., McConnell, M. L., Ryan, J. M. and Tousignant, O. (1997). Performance and simulation of cdznte strip detectors as submillimeter resolution imaging gamma radiation spectrometers, *IEEE Transactions on Nuclear Science* **44**(3): 922–928.

McGregor, D. and Hermon, H. (1997). Room-temperature compound semiconductor radiation detectors, *Nuclear Instruments and Methods in Physics Research Section A: Accelerators, Spectrometers, Detectors and Associated Equipment* **395**(1): 101 – 124.

Myronakis, M. E. and Darambara, D. G. (2011). Monte carlo investigation of charge-transport effects on energy resolution and detection efficiency of pixelated CZT detectors for SPECT/PET applications, *Medical Physics* **38**(1): 455–467.

NEMA (2013). *NEMA standards publication NU 1-2012: Performance measurements of gamma cameras*, National Electrical Manufacturers Association, Rosslyn, Virginia, USA.

Ogawa, K., Harata, Y., Ichihara, T., Kubo, A. and Hashimoto, S. (1991). A practical method for position-dependent Compton-scatter correction in single photon emission CT, *IEEE Transactions on Medical Imaging* **10**(3): 408–412.

Ogawa, K., Paek, S., Nakajima, M., Yuta, S., Kubo, A. and Hashimoto, S. (1988). Correction of collimator aperture using a shift-variant deconvolution filter in gamma camera emission CT, *in* S. J. D. III and R. H. Schneider (eds), *Medical Imaging II*, Vol. 0914, International Society for Optics and Photonics, SPIE, pp. 699–706.

Olcott, P. D., Habte, F., Foudray, A. M. and Levin, C. S. (2007). Performance characterization of a miniature, high sensitivity gamma ray camera, *IEEE Transactions on Nuclear Science* **54**(5): 1492–1497.

Ortega, J., Ferrer-Rebolleda, J., Cassinello, N. and Lledo, S. (2007). Potential role of a new hand-held miniature gamma camera in performing minimally invasive parathyroidectomy, *European Journal of Nuclear Medicine and Molecular Imaging* **34**(2): 165–169.

Owens, A. and Peacock, A. (2004). Compound semiconductor radiation detectors, *Nuclear Instruments and Methods in Physics Research Section A: Accelerators, Spectrometers, Detectors and Associated Equipment* **531**(1): 18 – 37.

Pais, H. L., Alho, I., Vendrell, I., Mansinho, A. and Costa, L. (2017). Radionuclides in oncology clinical practice–review of the literature, *Dalton Transactions* **46**(42): 14475–14487.

Pauwels, S., Barone, R., Walrand, S., Borson-Chazot, F., Valkema, R., Kvols, L. K., Krenning, E. P. and Jamar, F. (2005). Practical dosimetry of peptide receptor radionuclide therapy with 90Y-labeled somatostatin analogs, *Journal of Nuclear Medicine* **46**(1 suppl): 92S–98S.

Peterson, T. E. and Furenlid, L. R. (2011). SPECT detectors: the Anger camera and beyond, *Physics in Medicine and Biology* **56**(17): R145–R182.

Popovic, K., McKisson, J. E., Kross, B., Lee, S., McKisson, J., Weisenberger, A. G., Proffitt, J., Stolin, A., Majewski, S. and Williams, M. B. (2014). Development and characterization of a round hand-held silicon photomultiplier based gamma camera for intraoperative imaging, *IEEE Transactions on Nuclear Science* **61**(3): 1084–1091.

Press, W. H., Teukolsky, S. A., Vetterling, W. T. and Flannery, B. P. (2007). *Numerical recipes 3rd edition: The art of scientific computing*, Cambridge university press.

Pretorius, P. H., King, M. A., Pan, T.-S., de Vries, D. J., Glick, S. J. and Byrne, C. L. (1998). Reducing the influence of the partial volume effect on SPECT activity quantitation with 3D modelling of spatial resolution in iterative reconstruction, *Physics in Medicine and Biology* **43**(2): 407–420.

Pretorius, P. H., Liu, C., Fan, P., Peterson, M. and Ljungberg, M. (2015). Monte carlo simulations of the GE Discovery Alcyone CZT SPECT systems, *IEEE Transactions on Nuclear Science* **62**(3): 832–839.

Prettyman, T. (1999). Method for mapping charge pulses in semiconductor radiation detectors, *Nuclear Instruments and Methods in Physics Research Section A: Accelerators, Spectrometers, Detectors and Associated Equipment* **422**(1): 232 – 237.

Prettyman, T. H., Ameduri, F. P., Burger, A., Gregory, J. C., Hoffbauer, M. A., Majerus, P. R., Reisenfeld, D. B., Soldner, S. E. and Szeles, C. (2001). Effect of surfaces on the performance of CdZnTe detectors, *in* R. B. James (ed.), *Hard X-Ray and Gamma-Ray Detector Physics III*, Vol. 4507, International Society for Optics and Photonics, SPIE, pp. 23 – 31.

Ramo, S. (1939). Currents induced by electron motion, *Proceedings of the IRE* **27**(9): 584–585.

Richter, R. H., Andricek, L., Gebhart, T., Hauff, D., Kemmer, J., Lutz, G., Weiβ, R. and Rolf, A. (1996). Strip detector design for ATLAS and HERA-B using two-dimensional device simulation, *Nuclear Instruments and Methods in Physics Research Section A: Accelerators, Spectrometers, Detectors and Associated Equipment* **377**(2): 412–421. Proceedings of the Seventh European Symposium on Semiconductor.

Rogers, D. and Bielajew, A. (1990). 5 - monte carlo techniques of electron and photon transport for radiation dosimetry, *in* K. R. Kase, B. E. Bjärngard and F. H. Attix (eds), *The Dosimetry of Ionizing Radiation*, Academic Press, San Diego, pp. 427–539.

Rogowska, J. (2000). Overview and fundamentals of medical image segmentation, *in* I. N. Bankman (ed.), *Handbook of Medical Imaging: Processing and Analysis*, Biomedical Engineering, Academic Press, San Diego, chapter 5, pp. 69 – 85.

Roth, D., Larsson, E., Sundlöv, A. and Sjögreen Gleisner, K. (2020). Characterisation of a hand-held CZT-based gamma camera for 177Lu imaging, *EJNMMI Physics* **7**(1): 46.

Sandstrom, M., Sundin, A. and Lubberink, M. (2019). Intrinsic or extrinsic uniformity maps using 177Lu on a GE Discovery 870 CZT gamma camera, *Journal of Nuclear Medicine* **60**(supplement 1): 1363.

Scopinaro, F., Tofani, A., di Santo, G., Di Pietro, B., Lombardi, A., Lo Russo, M., Soluri, A., Massari, R., Trotta, C. and Amanti, C. (2008). High-resolution, hand-held camera for sentinel-node detection, *Cancer Biotherapy and Radiopharmaceuticals* **23**(1): 43–52.

Segars, W. P., Bond, J., Frush, J., Hon, S., Eckersley, C., Williams, C. H., Feng, J., Tward, D. J., Ratnanather, J. T., Miller, M. I., Frush, D. and Samei, E. (2013). Population of anatomically variable 4D XCAT adult phantoms for imaging research and optimization, *Medical Physics* **40**(4): 043701–1–043701–11.

Segars, W. P., Sturgeon, G., Mendonca, S., Grimes, J. and Tsui, B. M. (2010). 4D XCAT phantom for multimodality imaging research, *Medical Physics* **37**(9): 4902–4915.

Shockley, W. (1938). Currents to conductors induced by a moving point charge, *Journal of Applied Physics* **9**(10): 635–636.

Sidambe, A., Judson, D., Colosimo, S. and Fox, P. (2019). Laser powder bed fusion of a pure tungsten ultra-fine single pinhole collimator for use in gamma ray detector characterisation, *International Journal of Refractory Metals and Hard Materials* **84**: 104998.

Siegel, J. A., Thomas, S. R., Stubbs, J. B., Stabin, M. G., Hays, M. T., Koral, K. F., Robertson, J. S., Howell, R. W., Wessels, B. W., Fisher, D. R., Weber, D. A. and Brill, A. B. (1999). MIRD pamphlet no. 16: Techniques for quantitative radiopharmaceutical biodistribution data acquisition and analysis for use in human radiation dose estimates, *Journal of Nuclear Medicine* **40**(2): 37S–61S.

Siman, W. and Cheenu Kappadath, S. (2012). Performance characteristics of a new pixelated portable gamma camera, *Medical Physics* **39**(6): 3435–3444.

Sjögreen Gleisner, K. (2012). Scatter correction by deconvolution of planar whole-body scintillation-camera images using an image-based estimate of the signal-to-noise ratio, *European Journal of Nuclear Medicine and Molecular Imaging*, Vol. 39 (Suppl 2), p. S313. [abstract].

Sjögreen Gleisner, K. and Ljungberg, M. (2012). Patient-specific whole-body attenuation correction maps from a CT system for conjugate-view-based activity quantification: Method development and evaluation, *Cancer Biotherapy and Radiopharmaceuticals* **27**(10): 652–664.

Sjögreen Gleisner, K., Spezi, E., Solny, P., Gabina, P. M., Cicone, F., Stokke, C., Chiesa, C., Paphiti, M., Brans, B., Sandström, M., Tipping, J., Konijnenberg, M. and Flux, G. (2017). Variations in the practice of molecular radiotherapy and implementation of dosimetry: results from a European survey, *EJNMMI Physics* **4**(1): 28.

Snyder, W. S., Fisher, H. L. J., Ford, M. R. and Warner, G. G. (1969). Estimates of absorbed fractions for monoenergetic photon sources uniformly distributed in various organs of a heterogeneous phantom., *Journal of nuclear medicine* pp. Suppl 3:7–52.

Strand, S.-E. and Persson, B. R. R. (1977). The dual photopeak-area method applied to scintillation camera measurements of effective depth and activity of in vivo 123I-distributions, *European Journal of Nuclear Medicine* **2**(2): 121–128.

Strosberg, J., El-Haddad, G., Wolin, E., Hendifar, A., Yao, J., Chasen, B., Mittra, E., Kunz, P. L., Kulke, M. H., Jacene, H., Bushnell, D., O'Dorisio, T. M., Baum, R. P., Kulkarni, H. R., Caplin, M., Lebtahi, R., Hobday, T., Delpassand, E., Van Cut-sem, E., Benson, A., Srirajaskanthan, R., Pavel, M., Mora, J., Berlin, J., Grande, E., Reed, N., Seregni, E., Öberg, K., Lopera Sierra, M., Santoro, P., Thevenet, T., Erion, J. L., Ruszniewski, P., Kwekkeboom, D. and Krenning, E. (2017). Phase 3 trial of 177Lu-Dotatate for midgut neuroendocrine tumors, *New England Journal of Medicine* **376**(2): 125–135.

Sundlöv, A., Sjögreen-Gleisner, K., Svensson, J., Ljungberg, M., Olsson, T., Bernhardt, P. and Tennvall, J. (2017). Individualised 177Lu-DOTATATE treatment of neuroendocrine tumours based on kidney dosimetry, *European Journal of Nuclear Medicine and Molecular Imaging* pp. 1–10.

Sundlöv, A., Gustafsson, J., Brolin, G., Mortensen, N., Hermann, R., Bernhardt, P., Svensson, J., Ljungberg, M., Tennvall, J. and Sjögreen Gleisner, K. (2018). Feasibility of simplifying renal dosimetry in 177Lu peptide receptor radionuclide therapy, *EJNMMI Physics* **5**(1): 12.

Sundlöv, A., Sjögreen-Gleisner, K., Tennvall, J., Dahl, L., Svensson, J., Åkesson, A., Bernhardt, P. and Lindgren, O. (2021). Pituitary function after high-dose ^{177}Lu-DOTATATE therapy and long-term follow-up, *Neuroendocrinology* **111**(4): 344–353.

Svensson, J., Rydén, T., Hagmarker, L., Hemmingsson, J., Wängberg, B. and Bernhardt, P. (2016). A novel planar image-based method for bone marrow dosimetry in 177Lu-DOTATATE treatment correlates with haematological toxicity, *EJNMMI Physics* **3**(1).

Takeuchi, W., Suzuki, A., Shiga, T., Kubo, N., Morimoto, Y., Ueno, Y., Kobashi, K., Umegaki, K. and Tamaki, N. (2016). Simultaneous Tc-99m and I-123 dual-radionuclide imaging with a solid-state detector-based brain-SPECT system and energy-based scatter correction, *EJNMMI Physics* **3**(1): 10.

Thomas, B. A., Cuplov, V., Bousse, A., Mendes, A., Thielemans, K., Hutton, B. F. and Erlandsson, K. (2016). PETPVC: a toolbox for performing partial volume correction techniques in positron emission tomography, *Physics in Medicine and Biology* **61**(22): 7975–7993.

Tousignant, O., Hamel, L. A. and Vasilevski, D. (2000). Weighting potentials in CdZnTe γ-ray detectors with segmented electrodes, *IEEE Transactions on Nuclear Science* **47**(6): 2084–2086.

Vadawale, S., Purohit, S., Shanmugam, M., Acharya, Y., Goswami, J., Sudhakar, M. and Sreekumar, P. (2009). Characterization and selection of CZT detector modules for HEX experiment onboard Chandrayaan-1, *Nuclear Instruments and Methods in Physics Research Section A: Accelerators, Spectrometers, Detectors and Associated Equipment* **598**(2): 485 – 495.

Verger, L., Bonnefoy, J. P., Glasser, F. and Ouvrier-Buffet, P. (1997). New developments in CdTe and CdZnTe detectors for x and γ-ray applications, *Journal of Electronic Materials* **26**(6): 738–744.

Vorwerk, H., Beckmann, G., Bremer, M., Degen, M., Dietl, B., Fietkau, R., Gsänger, T., Hermann, R. M., Herrmann, M. K. A., Höller, U., van Kampen, M., Körber, W., Maier, B., Martin, T., Metz, M., Richter, R., Siekmeyer, B., Steder, M., Wagner, D., Hess, C. F., Weiss, E. and Christiansen, H. (2009). The delineation of target volumes for radiotherapy of lung cancer patients, *Radiotherapy and Oncology* **91**(3): 455 – 460.

Walrand, S., Barone, R., Pauwels, S. and Jamar, F. (2011). Experimental facts supporting a red marrow uptake due to radiometal transchelation in 90Y-DOTATOC therapy and relationship to the decrease of platelet counts, *European Journal of Nuclear Medicine and Molecular Imaging* **38**(7): 1270–1280.

Zhang, F. and He, Z. (2004). 3D position-sensitive CdZnTe gamma-ray spectrometers: improved performance with new ASICs, *in* A. Burger, R. B. James and L. A. Franks (eds), *Hard X-Ray and Gamma-Ray Detector Physics VI*, Vol. 5540, International Society for Optics and Photonics, SPIE, pp. 135 – 143.

Zhang, T., Du, Y., Pan, F., Tkaczyk, J. E., Chen, H. and Bindley, G. (2011). Low cost, thick CZT spectroscopic detectors by sensor-pack construction of multiple tile pieces, *2011 IEEE Nuclear Science Symposium Conference Record*, pp. 4838–4843.

Department of Medical Radiation Physics
Faculty of Science
Lund University

LUND
UNIVERSITY